Chem Soc Rev

REVIEW ARTICLE

View Article Online
View Journal | View Issue

Cite this: *Chem. Soc. Rev.*, 2025, **54**, 11699

Combining quantum chemistry, machine learning and rate theory for organic luminescent materials

Rongrong Li,[a] Qi Ou*[b] and Zhigang Shuai *[ac]

The theoretical design of highly efficient, low roll-off and full-color emission organic materials is of great interest, although there are great challenges due to the limitations of the present-day methodology. In this review, we present progress achieved in our group on the theoretical and computational investigation for the structure–property relationships and screening strategy for organic fluorescent molecules, selection of thermally activated delayed fluorescence (TADF) and multi-resonance TADF (MR-TADF) molecules for optically and electrically pumped lasing application, and high-throughput virtual screening of phosphorescent organometallic complexes. We combined a quantum chemistry method with the molecular representation learning model Uni-Mol and rate theory-based molecular material property prediction package (MOMAP) developed in our group. Finally, we outline the limitation of current computational protocols and the future directions for organic luminescent materials.

Received 12th August 2025

DOI: 10.1039/d5cs00959f

rsc.li/chem-soc-rev

1. Introduction

Since Tang and Slyke reported the first organic electroluminescent diode (OLED) in 1987, it quickly sparked research interest in OLEDs within both academia and industry.[1] Currently, OLEDs are widely applied in automotive displays, mobile phone screens, solid state lighting, and high-definition monitors.[2,3] As the core of OLED technology, organic luminescent materials have been a perennial research hotspot, given that their photoluminescence

[a] *Guangdong Basic Research Center of Excellence for Aggregate Science, School of Science and Engineering, The Chinese University of Hong Kong, Shenzhen, Guangdong, 518172, P. R. China. E-mail: shuaizhigang@cuhk.edu.cn*
[b] *SINOPEC Research Institute of Petroleum Processing Co., Ltd, Beijing 100083, P. R. China. E-mail: ouqi.ripp@sinopec.com*
[c] *MOE Key Laboratory for Organic Optoelectronics and Molecular Engineering, Department of Chemistry, Tsinghua University, Beijing 100084, P. R. China*

Rongrong Li

Rongrong Li received her BSc degree in Chemistry from Northeast Normal University in 2018 and earned her PhD degree from the Institute of Chemistry, Chinese Academy of Sciences in 2023, under the supervision of Prof. Xinzheng Yang. She is currently a postdoctoral fellow at the Chinese University of Hong Kong, Shenzhen, working with Prof. Zhigang Shuai. Her research focuses on the computational study of reaction mechanisms and the theoretical design of organic luminescent materials.

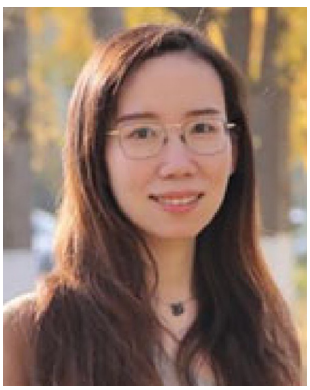

Qi Ou

Qi Ou received her BSc degree from the University of Science and Technology of China in 2011 and obtained her PhD in Chemistry from the University of Pennsylvania in 2017, supervised by Prof. Joseph Subotnik. After conducting post-doctoral research with Prof. Emily Carter at Princeton University (2017–2018) and with Prof. Zhigang Shuai at Tsinghua University (2019–2021), she became a research scientist at the AI For Science Institute (AISI), Beijing (2021–2023). In 2023, she joined the Sinopec Research Institute of Petroleum Processing Co. as a group leader. Her research focuses on the development of electronic structure tools and the rate theory of photophysical processes, as well as machine learning-based density functionals.

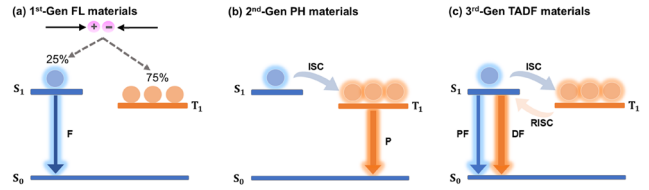

Fig. 1 Schematic emission mechanism of (a) the first-generation fluorescence materials, (b) the second-generation phosphorescence materials, and (c) the third-generation thermally activated delayed fluorescence materials.

quantum yield and color purity directly dictate the performance of display panels.[4–7]

The first-generation OLED materials are traditional fluorescent materials, which only utilize singlet excitons to emit light, resulting in a theoretical maximum internal quantum efficiency (IQE) of only 25% owing to spin statistics.[8] Due to optical losses occurring during photon out-coupling processes, such as waveguide effects, total internal reflection, and microcavity effects, the measured external quantum efficiency (EQE) is typically around 5%, far below the 25% threshold.[9–12] In order to improve the efficiency of OLED devices, it is of great significance to develop organic materials that can fully implement triplet exciton emission. Both phosphorescent materials and thermally activated delayed fluorescent (TADF) materials can effectively exploit triplet excitons, leading to nearly 100% IQE in theory and thereby boosting the EQEs.[13–16] The schematic emission mechanisms of the fluorescence materials, phosphorescence materials, and TADF materials are displayed in Fig. 1(a)–(c).

Most phosphorescent materials are inorganic compounds or expensive organometallic complexes.[17–19] Through the utilization of precious metals such as iridium, platinum, and ruthenium, the spin–orbital coupling (SOC) constant is enhanced *via* the heavy atom effect, leading to the acceleration of the intersystem crossing (ISC) process, which enables the spin–forbidden emission from the triplet excited state to the singlet ground state. However, the lack of stable blue phosphorescent emitters, the toxicity, and the high economic costs of noble metals dramatically hinder the application of phosphorescence materials.[20–22]

TADF materials harvest triplet excitons *via* reverse intersystem crossing (RISC), emitting delayed fluorescence (DF).[23–25] The upconversion of low-energy triplet states to high-energy singlet states is an endothermic process. Thus, a tiny singlet–triplet energy gap (ΔE_{ST}) is the prerequisite of efficient RISC. Reducing the overlap between the highest occupied molecular orbital (HOMO) and the lowest unoccupied molecular orbital (LUMO) leads to a smaller ΔE_{ST} value, which can be accomplished by the rigid and spatially twisted molecular structure.[26–30] Furthermore, enhancing SOC can effectively promote the RISC process. Generally, the singlet state of the TADF molecule possesses a charge transfer (CT) transition, requiring the triplet excited state to be primarily a locally excited (LE) state to achieve a larger SOC based on the El-Sayed rule.[31–35] While the CT emission has a small transition dipole and low oscillator strength, the LE emission has large transition dipoles and high oscillator strength, which indicates that it is important to get a balance between the SOC and singlet oscillator strength.[36,37] Therefore, a rational molecular structure design is necessary to attain a smaller ΔE_{ST} and an effective RISC. In 2016, multi-resonance thermally activated delayed fluorescence (MR-TADF) molecules were proposed by Hatakeyama *et al.*[38] The locally separated frontier molecular orbitals of the MR-TADF molecules indicated a relatively large oscillator strength as compared to the conventional TADF molecules while maintaining the small ΔE_{ST}, making these molecular systems promising candidates for future OLED materials. Furthermore, Adachi *et al.* proposed ''hyperfluorescence'', in which fluorescent emitters and TADF molecules as sensitizers are co-embedded into a host matrix.[39–42] This approach enables narrowband emission and mitigates efficiency roll-off by facilitating the transfer of excitons generated on the TADF sensitizers to the fluorescent emitters. Hyperfluorescent OLEDs have been considered as fourth-generation OLED devices. Additionally, materials exhibiting an inverted singlet–triplet energy gap (INVEST), where the energy of the first excited singlet state lies below that of the lowest triplet state, have been reported.[43–45] Such energy ordering significantly enhances the RISC process, enabling the highly efficient conversion of triplet excitons into singlet excitons and holding the promise of 100% IQE.

Density functional theory (DFT) and time-dependent density functional theory (TD-DFT) are currently the most widely used

Zhigang Shuai

Zhigang Shuai is the X. Q. Deng Presidential Chair Professor at the Chinese University of Hong Kong–Shenzhen since 2022. He received his BSc degree in 1983 from Sun Yat–Sen University and PhD degree in 1989 from Fudan University. After conducting postdoctoral research with Prof. Jean–Luc Brédas at the University of Mons, Belgium, he joined the Institute of Chemistry, Chinese Academy of Sciences, under the ''Hundred–Talent Program'' in 2002. He moved to Tsinghua University in 2008 as a Changjiang Scholar Chair Professor. He has been working on developing computational methods for modelling excited state structures and dynamics in organic and polymeric materials. He developed the quantum chemistry density matrix renormalization group theory and its time-dependent formalism for electronic structure and quantum dynamics for complex systems. He has led the development of the commercial software MOMAP. He has published over 470 papers and has an H-index of 99. He is an elected member of the Royal Academy of Belgium, International Academy of Quantum Molecular Science, Academia Europaea, and the Scientific Board of the World Association of Theoretical and Computational Chemistry.

computational tools for evaluating the ground state and excited state structures, energies, and properties of most organic and inorganic dye molecules.[46–49] These methods with the formal scaling of $O(N^3)$, where N represents the system size in terms of the number of basis functions, not only have moderate computational costs but also take into account the influence of the environment by the polarizable continuum model (PCM) or using multiple QM/MM approaches. Nevertheless, meaningful prediction results can only be obtained through extensive benchmark calculations with functional selection. Compared to the excellent performance for traditional organic luminescent molecules, TD-DFT encounters considerable difficulties in predicting the emission energy of TADF and MR-TADF molecules due to the spurious consideration of the CT state[50] and/or electron correlation.[51,52] Although correlated wavefunction methods that include higher-order electronic excitations can achieve higher computational accuracy, they also lead to a significant increase in computational time.[53,54] For example, the equation-of-motion coupled-cluster singles and doubles (EOM-CCSD) scales formally with $O(N^6)$. Olivier *et al.* reported that the wavefunction-based method, spin-component scaling second-order approximate coupled cluster (SCS-CC2), has a mean average deviation (MAD) of 0.04 eV for the predicted ΔE_{ST} of MR-TADF molecules, and the computational time can be reduced somewhat to $O(N^5)$.[55] Subsequently, a large number of methods incorporating double excitations, such as the second-order algebraic diagrammatic construction [ADC(2)], SCS-ADC(2), and spin-opposite scaled CC2 (SOS-CC2), have also been successfully applied to the excited state energy calculation of MR-TADF molecules.[56,57]

Theoretical studies of organic luminescent materials have played a key role in revealing their photophysical mechanisms, optimizing the molecular design, and improving the device performance.[58–62] While the combination of quantum chemistry (QC), machine learning (ML), and rate theory presents a promising paradigm, the seamless integration of these multiscale methods to build a predictive and interpretable bridge from the molecular structure to device performance remains a central challenge. This review does not attempt to provide an encyclopedic account of all related works. Instead, through the lens of our group's systematic explorations at this intersection, we aim to chart a viable pathway from a fundamental physical understanding to an efficient material design. We will critically examine: (1) how rigorous benchmarking leads to the selection of 'fit-for-purpose' computational methods, balancing accuracy and efficiency for different luminescent systems; (2) how complex photophysical dynamics can be distilled into computable descriptors to enable a leap from understanding to predicting; and (3) how ML is reshaping traditional high-throughput virtual screening. We hope that the case studies presented herein provide a research framework that is both theoretically profound and practically instructive. This review is organized as follows. Section 2 introduces the thermal vibration correlation functions (TVCF) for photophysical properties evaluation and Uni-mol model for high-throughput virtual screening (HTVS). Section 3 mainly presents the screen-out protocol of organic fluorescent molecules, TADF, and MR-TADF molecules for lasing application, respectively. Section 4 describes the phosphorescence spectral prediction and automatic screening workflow of phosphorescent organometallic complexes. Section 5 is the summary and outlook.

2. Computational methodologies

2.1 The evaluation of photophysical properties based on thermal vibration correlation functions

The accurate and quantitative prediction of the photoluminescence quantum yield (PLQY) of organic luminescent molecules is a pressing yet challenging task. The difficulties in calculating the spectra, radiative and non-radiative rates lie in handling the electron–vibrational coupling between the ground and excited states, as well as the resulting changes in equilibrium configurations, which determines the displacement of normal modes, Huang–Rhys factors, and the magnitude of reorganization energy and the rotational effects between vibrational modes. The traditional displacement harmonic oscillator model ignores the rotational effect between normal modes, making it difficult to accurately quantify the photophysical processes. Building upon the harmonic approximation and comprehensively accounting for the normal mode displacements and mode rotation effects between different potential energy surfaces, analytical expressions for the spectra, radiative, and non-radiative rates based on TVCF are derived by treating non-adiabatic coupling and spin–orbit coupling as perturbations.[63–65]

For the calculation of the radiative rate constant k_r, based on Einstein's formula for spontaneous emission, different vibrational level distributions are further considered. The calculation formula is as follows:

$$k_r(T) = \int \sigma_{em}(\omega, T)\mathrm{d}\omega \tag{1}$$

$$\sigma_{em}(\omega, T) = \frac{2\omega^3}{3\pi\hbar c^3}|\mu_{fi}|^2 \int_{-\infty}^{+\infty} e^{-i(\omega-\omega_{if})t}\rho_{em}(t, T)\mathrm{d}t \tag{2}$$

where $\sigma_{em}(\omega, T)$ is the emission spectrum, μ_{fi} is the electric transition dipole moment between the final and initial electronic states, describing the strength and directionality of an electronic transition between two states, $\rho_{em}(t, T) = Z_i^{-1}\mathrm{Tr}(e^{-i\tau_f\hat{H}_f}e^{-i\tau_i\hat{H}_i})$ is the TVCFs, $Z_i = \sum_{v=0}^{\infty} e^{-\beta E_{iv}}$ is the partition function for the vibrational normal mode, β is the reciprocal of temperature T times Boltzmann constant k_B, $\tau_i = -i\beta - t/\hbar$ and $\tau_f = t/\hbar$, and $\hat{H}_f$ and $\hat{H}_i$ is the harmonic oscillator Hamiltonian of the final and initial electronic states, respectively. Within the framework of Fermi's golden rule and second-order perturbation theory, the general expression for the non-radiative transition rate constant can be written as:

$$k_{f\leftarrow i} \equiv \frac{2\pi}{\hbar}\sum_{v,\mu} P_{i\nu}\left|H'_{fu,i\nu} + \sum_{n,\mu}\frac{H'_{fu,n\mu}H'_{n\mu,i\nu}}{E_{i\nu} - E_{n\mu}}\right|^2 \delta(E_{i\nu} - E_{f\mu}) \tag{3}$$

where $P_{i\nu} = \frac{e^{-\beta E_{iv}}}{Z_i}$ is the Boltzmann distribution function,

$\delta(E_{i\nu} - E_{f\mu}) = \frac{\hbar}{2\pi}\int_{-\infty}^{+\infty} d\tau\, e^{-i(E_{i\nu}-E_{f\mu})\tau}$, $\tau = t/\hbar$, the perturbation term H' represents the interaction between two different Born–Oppenheimer states, and consists of the non-adiabatic coupling term $\hat{H}^{BO}$ and the spin–orbit coupling term $\hat{H}^{SO}$, with the following form:

$$\hat{H}'\Psi_{i\nu} = \hat{H}^{BO}\Phi_i(\boldsymbol{r};\boldsymbol{Q})\Theta_\nu(\boldsymbol{Q}) + \hat{H}^{SO}\Phi_i(\boldsymbol{r};\boldsymbol{Q})\Theta_\nu(\boldsymbol{Q}) \quad (4)$$

where Φ_i and Θ_ν are the electronic and vibrational wavefunctions, respectively. For the photophysical processes of electron spin conservation, such as singlet internal conversion, the rate constant can be obtained from first-order perturbation theory:

$$k_{ic} = \frac{1}{\hbar^2}\sum_{kl} R_{kl}\int_{-\infty}^{+\infty} e^{i\omega_{if}t}\rho_{fi,kl}^{ic}(t,T)dt \quad (5)$$

where R_{kl} represents the non-adiabatic coupling between two electronic states Φ_f and Φ_i, $R_{kl} = \langle\Phi_f|\hat{P}_{fk}|\Phi_i\rangle\langle\Phi_i|\hat{P}_{fl}|\Phi_f\rangle$, $\hat{P}_{fk}$ and $\hat{P}_{fl}$ are the nuclear momentum operators for the corresponding vibrational normal modes, and $\rho_{fi,kl}^{ic}$ is the internal conversion correlation function, $\rho_{fi,kl}^{ic}(t,T) = Z_i^{-1}\mathrm{Tr}(\hat{P}_{fk}e^{-i\tau_f\hat{H}_f}e^{-i\tau_i\hat{H}_i})$. For the ISC and RISC processes, where the electron spin changes between singlet and triplet states, the mechanism is primarily driven by spin–orbit coupling. Therefore, only the spin–orbit coupling term $\hat{H}^{SO}$ is effective, and the corresponding rate constant should be expressed as:

$$k_{isc/risc} = \frac{1}{\hbar^2}\left|H_{fi}^{SO}\right|^2\int_{-\infty}^{+\infty} e^{i\omega_{if}t}\rho_{fi}^{isc/risc}(t,T)dt \quad (6)$$

Similarly, $\rho_{fi}^{isc/risc}(t,T) = Z_i^{-1}\mathrm{Tr}(e^{-i\tau_f\hat{H}_f}e^{-i\tau_i\hat{H}_i})$ is the ISC/RISC correlation function. The calculation of the rate constant for the non-radiative transition from the triplet state to the ground state is similar. Based on the above theoretical foundation, the molecular materials property prediction package (MOMAP) software has been developed. All input parameters required in the above theoretical formulas can be obtained using modern quantum chemistry software, such as Gaussian,[66] ORCA,[67] and QChem,[68] without the need for any empirical parameters. All photophysical properties introduced in this work, including absorption and emission spectra, as well as various rate constants, are computed using MOMAP.

2.2 Uni-mol model for high-throughput virtual screening

The design and discovery of new molecules rely on professional knowledge, experimental verification, as well as trial-and-error processes, which require considerable expenditure. Thanks to the rapid development of large-scale computing resources, advanced simulation and theoretical algorithms, HTVS has become a breakthrough tool in the design of new materials. HTVS has successfully predicted the most promising experimental validation candidates by comprehensively exploring chemical spaces with customized properties, and can significantly reduce trial-and-error costs. Machine learning (ML) algorithms, as a powerful tool, effectively predict experimental or quantum mechanical (QM) characteristics and significantly reduce data generation consumptions by constructing quantitative structure–activity relationships (QSAR). However, the early ML algorithms for property prediction apply the manually selected structural features as descriptors, requiring case-by-case designs for different systems. The recently developed Uni-Mol is a molecular representation learning (MRL) scheme that further improves data efficiency by using unlabeled data as prior knowledge.[69]

Unlike other MRL models that deal with representing molecules as 1D sequence strings (such as SMILES, InChI) and 2D graphs, Uni-Mol possesses a general 3D molecular pretraining framework and is capable of directly taking 3D coordinates as inputs and outputs. The structure of Uni-mol includes three parts: backbone, pretraining and finetune. The default transformer backbone without positional encoding cannot distinguish the positions in 3D space. Therefore, the relative positional encoding is added using Euclidean distances of all atom pairs and pair-type aware Gaussian kernels in Uni-mol. The D-channel positional encoding for atom pair ij is expressed as:

$$\begin{aligned}\boldsymbol{p}_{ij} &= \left\{\mathcal{G}\left(\mathcal{A}\left(d_{ij},t_{ij};\boldsymbol{a},\boldsymbol{b}\right),\mu^k,\sigma^k\right)\middle|k\in[1,D]\right\},\\ \mathcal{A}(d,r;\boldsymbol{a},\boldsymbol{b}) &= a_r d + b_r\end{aligned} \quad (7)$$

where $\mathcal{G}(d,\mu,\sigma) = \frac{1}{\sigma\sqrt{2\pi}}e^{-\frac{(d-\mu)^2}{2\sigma^2}}$ is the Gaussian density function, d_{ij} and t_{ij} are the Euclidean distance and pair-type of atom pair ij, respectively, and $\mathcal{A}\left(d_{ij},t_{ij};\boldsymbol{a},\boldsymbol{b}\right)$ is the affine transformation. All parameters except d_{ij} and t_{ij} are trainable and randomly initialized. Then, the atom-to-pair communication by multi-head Query-key product is used for updating the pair representation. The update of ij pair representation is denoted as:

$$\boldsymbol{q}_{ij}^0 = \boldsymbol{p}_{ij}\boldsymbol{M},\quad \boldsymbol{q}_{ij}^{l+1} = \boldsymbol{q}_{ij}^l + \left\{\frac{\boldsymbol{Q}_i^{l,h}\left(\boldsymbol{K}_j^{l,h}\right)^T}{\sqrt{d}}\middle|h\in[1,H]\right\} \quad (8)$$

where $\boldsymbol{q}_{ij}^l$ is the pair representation of the ij atom pair in the l-th layer, H is the attention head number, d is the hidden representation dimension, $\boldsymbol{Q}_i^{l,h}(\boldsymbol{K}_j^{l,h})$ is the Query(Key) of i-th (j-th) atom in the l-th layer and h-th head, and $\boldsymbol{M}\in\mathbb{R}^{D\times H}$ is the projection matrix. In addition, to fully utilize the 3D information in the atom representation, the pair-to-atom communication using pair representation as bias terms in self-attention is introduced, and expressed as follows:

$$\mathrm{Attention}\left(\boldsymbol{Q}_i^{l,h},\boldsymbol{K}_j^{l,h},\boldsymbol{V}_j^{l,h}\right) = \mathrm{softmax}\left(\frac{\boldsymbol{Q}_i^{l,h}\left(\boldsymbol{K}_j^{l,h}\right)^T}{\sqrt{d}} + \boldsymbol{q}_{i,j}^{l-1,h}\right)\boldsymbol{V}_j^{l,h} \quad (9)$$

where $\boldsymbol{V}_j^{l,h}$ is the value of the j-th atom in the l-th layer and h-th head. Finally, a simple SE(3)-equivariance head is added to directly output the 3D coordinates, expressed as:

$$\begin{aligned}\hat{\boldsymbol{x}}_i &= \boldsymbol{x}_i + \sum_{j=1}^{n}\frac{\left(\boldsymbol{x}_i-\boldsymbol{x}_j\right)c_{ij}}{n},\\ c_{ij} &= \mathrm{ReLU}\left(\left(\boldsymbol{q}_{ij}^L - \boldsymbol{q}_{ij}^0\right)\boldsymbol{U}\right)\boldsymbol{W}\end{aligned} \quad (10)$$

where n is the total atom number, L is the layer number, $\boldsymbol{x}_i\in\mathbb{R}^3$

is the coordinate input, $\hat{\boldsymbol{x}}_i \in \mathbb{R}^3$ is the output coordinate, ReLU(y) = max(0, y) is the Rectified Linear Unit, and $\boldsymbol{U} \in \mathbb{R}^{H\times H}$ and $W \in \mathbb{R}^{H\times 1}$ are project matrices to transform the pair representation to scalar, respectively. The Uni-Mol model has been widely applied in fields such as molecular modeling, drug discovery, and materials design, and some of the predicted organic molecules have already been synthesized experimentally.

3. Organic fluorescent materials for lasing

Laser technology, as the mainstream of next-generation display innovations, has captured the spotlight in the field of optoelectronics in recent years. The development of laser gain media is crucial for the advancement of laser technology. Compared with inorganic gain media, organic materials with the advantages of low cost and almost unlimited modifiability have attracted immense attention.[70,71] In this section, recent works with a systematic investigation of photophysical properties are introduced, which include a series of organic fluorescent molecules, TADF and MR-TADF molecules. The comparison between 12 organic laser molecules and 23 organic molecules without laser characteristics identifies the key to realize amplified spontaneous emission. Subsequently, the potential of TADF and MR-TADF materials for lasing applications is explored.

3.1 Excited-state properties and photophysical parameters.

The excited-state structures and photophysical properties of organic luminescent molecules are crucial for the performance of organic light-emitting diodes and laser emission. To accurately calculate and predict the photophysical properties of luminescent molecules, various studies have been conducted with the aim of identifying suitable methods for precisely simulating the excited-state electronic structures of these molecules. Jacquemin *et al.*[72] conducted a series of benchmark studies to evaluate the accuracy of TD-DFT for calculating excited states transition energies. A wide range of pure functionals, global hybrid (GH) functionals, and long-range corrected hybrid (LCH) functionals were tested on over 700 excited states. Using experimental data or high-accuracy wavefunction-based CASPT2/TZVP results as reference, the most accurate predictions are achieved using either GH functionals containing ~20% to 25% Hartree–Fock (% HF) exact exchange, such as B3LYP (20% HF),[73] PBE0 (25% HF),[74] and mPW1PW91 (25% HF),[75] or long-range corrected functionals with a small damping parameter, such as LC-ωPBE(20) (with ω = 0.20).[76] Gong *et al.*[77] calculated the excitation energies of eight triphenylamine-based molecules and compared them with experimental fluorescence spectra, showing that B3LYP is the optimal choice for these molecules, with a mean absolute error (MAE) of 0.09 eV. Ou *et al.*[78] reported a comprehensive calculation of 35 organic molecules, the results of which indicated that the MAE of emission energy calculated by B3LYP was also 0.09 eV. Troisi *et al.*[79] presented a systematic approach to evaluate 71 molecules. After assessing 18 different computational methods, the M06-2X/def2-TZVP[80] approach emerged as particularly effective, showing robust correlations between the calculated and experimental values for the excitation energy, oscillator strength, and exciton reorganization energy, with R^2 values of 0.948, 0.844, and 0.690, respectively. B3LYP shows the second-best linear correlation after M06-2X, with R^2 values of 0.906 for the excitation energy and 0.799 for the oscillator strength, respectively. Combining the above studies, TD-DFT with the B3LYP functional is a reliable approach for simulating the singlet excited state (S_1) of organic luminescent molecules.

Due to the poor description of the Coulomb correlation in TD-DFT, traditional hybrid functionals are unable to accurately calculate the excited states of TADF molecules with obvious CT characteristics, let alone those of MR-TADF molecules. Sun *et al.*[81] demonstrated that TD-DFT within the Tamm-Dancoff approximation (TDA) can successfully evaluate the ΔE_{ST} of TADF molecules. When applied to 17 molecules, the nonempirically tuned range-separated functional LC-ω*PBE yields a MAE of 0.07 eV compared to the corresponding experimental values. Lin *et al.*[82] reported that for simulated TADF molecules, the MAE of emission energy and ΔE_{ST} between ωB97XD[83] calculations and experimental values was 0.117 eV and 0.111 eV, respectively. Olivier *et al.*[84] found that the use of TDA in combination with CAM-B3LYP,[85] M06-2X, and two ω-tuned range-separated functionals, LC-ω*PBE and LC-ω*HPBE,[86] obtained the best agreement with the SCS-CC2 calculations in the prediction of ΔE_{ST} (MAE ~ 0.12 eV). Furthermore, CAM-B3LYP and M06-2X perform well in calculating the excited energies of S_1, T_1 and T_2, with the MAE around 0.12 eV, while the corresponding MAE for LC-ω*PBE and LC-ω*HPBE, are around 0.50 eV. Therefore, it is recommended to use ω-tuned range-separated functionals, such as LC-ω*PBE, for calculating the ΔE_{ST} of TADF molecules, and ωB97XD, M06-2X or CAM-B3LYP for predicting their S_1 excitation energies.

The significant contribution of double excitations of MR-TADF systems makes the TD-DFT method no longer suitable for calculating their excited states. However, methods that include higher-order excitations (such as double, triple, *etc.*) are computationally expensive, and thus unsuitable for studying large sets of molecules or large molecular systems. In addition to the SCS-CC2 mentioned in the introduction section, Sanyam *et al.*[87] reported that the double-hybrid functional B2PLYP[88] and the highly correlated wavefunction-based STEOM-DLPNO–CCSD method can achieve a good balance of ΔE_{ST} evaluation for MR-TADF molecules, with ~0.06 eV MAE. For the calculation of MR-TADF molecules, more convenient and efficient computational methods for applications such as high-throughput screening remain to be further explored.

Synthesizing the literature and our own practical experience, we can outline a 'decision tree' for selecting computational methods for organic luminescent materials in Fig. 2. For conventional fluorescent small molecules, TD-DFT with functionals like B3LYP, PBE0, or M06-2X offers the best balance of accuracy and efficiency, serving as a reliable workhorse. However, as systems extend to TADF molecules with pronounced CT character, the limitations of conventional functionals become

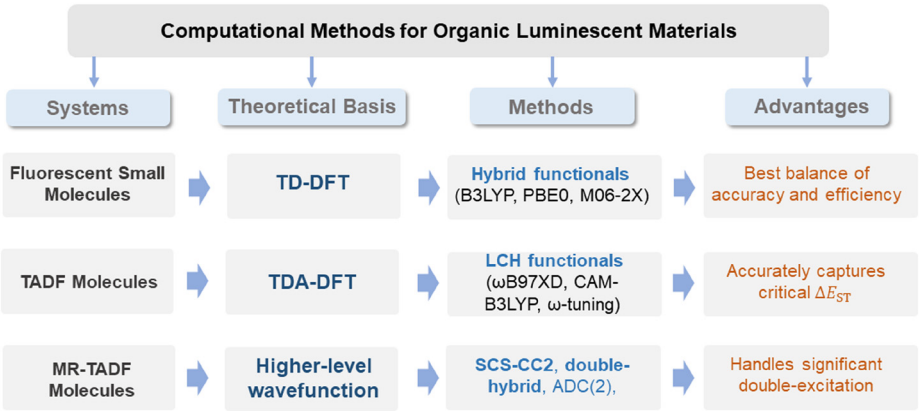

Fig. 2 Selection of computational methods for organic luminescent materials.

apparent, necessitating a shift to long-range corrected functionals like ωB97XD or CAM-B3LYP, or even system-specific ω-tuning, to accurately capture the critical ΔE_{ST}. For the frontier MR-TADF systems, the significant double-excitation character renders most TD-DFT methods inadequate, compelling the use of higher-level wavefunction methods such as SCS-CC2, ADC(2), or double-hybrid functionals, albeit at a significantly increased computational cost. This hierarchical strategy underscores a central tenet: there is no universal computational method. A profound understanding of the underlying luminescence mechanism is the prerequisite for selecting the right tool. This reality also motivates the future development of more efficient and universally applicable computational schemes for complex excited states.

3.2 Screening scheme for electrically pumped organic laser molecules

Based on the accurate computational simulations of organic luminescent molecules *via* QM methodologies, ref. 78 carried out a screening of organic fluorescent lasing materials. Fig. 3 displays the investigated molecular structures.[89–116] The S_0, S_1, T_1, and polarons with positive and negative charge as cations and anions ($D_0^{+/-}$), which involves laser emission, are optimized *via* restricted DFT, TD-DFT and unrestricted DFT (UDFT) method, respectively.[117–121] The oscillator strength, theoretical photophysical properties and computational and experimental PLQY are shown in Table 1. Different photophysical rate constants were all calculated by our MOMAP software.[63–65] The MAE of the calculated PLQY value is about 10% when compared with the experimental results, indicating a reasonable prediction of TVCF.

The first screening criterion applied in ref. 78 is the oscillator strength, which is directly proportional to the emission cross section σ_{em} *via*:[122]

$$\sigma_{em}(\upsilon) = \frac{e^2}{4\varepsilon_0 m_e c_0 n_F} g(\upsilon) f_{em}, \quad (11)$$

where υ is the corresponding emission frequency, ε_0 is the vacuum permittivity, m_e is the electron mass, c_0 is the light speed, n_F is the refractive index of the gain material, e is the electron charge, and $g(\upsilon)$ is the normalized line shape Gaussian function with $\int g(\upsilon)d\upsilon = 1$. The preliminary screening of laser molecules can be achieved by excluding the molecules with small f_{em}. As shown in Table 1, all selected 12 optical pumping materials with low laser or amplified spontaneous emission (ASE) thresholds have a large emission oscillator strength ($f_{em} > 0.5$). The stimulated emission cross section is evaluated through eqn (11) and by inserting $g(\upsilon) = \frac{g(\lambda)d\lambda}{d\upsilon} = g(\lambda)\frac{\lambda^2}{c_0}$ into eqn (11), and the σ_{em} is rewritten as a function of wavelength:

$$\sigma_{em}(\lambda) = \frac{e^2\lambda^2}{4\varepsilon_0 m_e c_0^2 n_F} g(\lambda) f_{em}, \quad (12)$$

where $g(\lambda)$ expressed in the emission wavelength domain is the normalized line shape Gaussian function, using the equation $\int g(\lambda)d\lambda = 1$. The absorption cross section σ_{abs} is similar to σ_{em}, where f_{em} is replaced by various absorption oscillator strengths $f_{abs}^{X_i \to X_j}$ ($X_i \to X_j = S_0 \to S_1$, $S_1 \to S_n$, $T_1 \to T_n$, and $D_0^{+/-} \to D_n^{+/-}$).[123] Furthermore, the optical pumping net emission cross-section $\sigma_{eff}^{net,opt}$ and electrical pumping net emission cross-section $\sigma_{eff}^{net,ele}$ are defined as eqn (13) and (14), respectively, *via*:

$$\sigma_{eff}^{net,opt} = \sigma_{em} - \sigma_{abs}^{S_0 \to S_1} - \sigma_{abs}^{S_1 \to S_n}, \quad (13)$$

$$\sigma_{eff}^{net,ele} = \sigma_{em} - \sigma_{abs}^{S_0 \to S_1} - \sigma_{abs}^{S_1 \to S_n} - \sigma_{abs}^{T_1 \to T_n} - \sigma_{abs}^{D_0^+ \to D_n^+} - \sigma_{abs}^{D_0^- \to D_n^-} \quad (14)$$

As depicted in eqn (13) and (14), $\sigma_{eff}^{net,opt}$ and $\sigma_{eff}^{net,ele}$ refer to the effective laser emission cross-sections after overcoming different absorption loss processes. All 12 molecules have positive and large optical pumping net emission cross-sections $\sigma_{eff}^{net,opt}$, as shown in Table 2, indicating that these molecules have great potential for laser emission. In fact, the laser behavior of these molecules has been demonstrated experimentally.[89–96,98,102] The computational results agree with the experiments, demonstrating that the method used in ref. 78 for laser cross-sections calculation is reliable.

The laser threshold power is described by $P^{th} = \frac{(\alpha_i + k)h\nu}{\sigma_{em}(\nu) \times \tau_{S_1}}$, where α_i is the internal loss, k is the cavity loss, h is Planck constant, ν is emission frequency, and τ_{S_1} is singlet lifetime. It

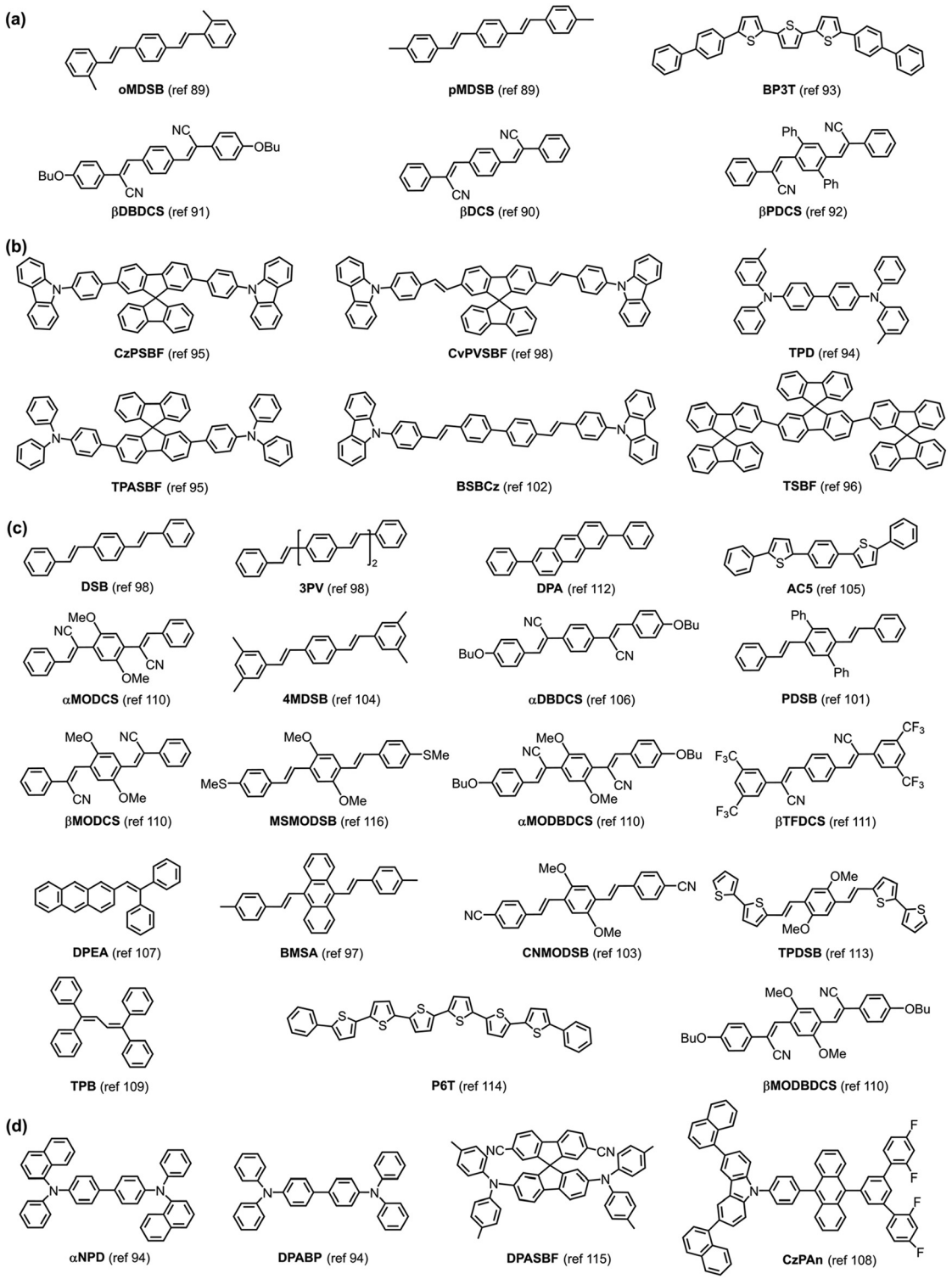

Fig. 3 The molecular structures of the investigated organic fluorescent materials. (a) and (c) The molecules are single crystal materials with and without laser properties, respectively. (b) and (d) The molecules are thin film organic fluorescent materials with and without laser properties, respectively. (a)–(d) are reproduced with permission from ref. 78. Copyright 2020 Springer Nature.

indicates that P^{th} is inversely proportional to the emission cross-section $\sigma_{em}(\upsilon)$ and singlet lifetime τ_{S_1}. The experimental threshold power P^{th} with respect to computational $1/(\sigma_{em}^{net,opt}\tau_{S_1})$ is plotted in Fig. 4(a). A good linear relationship with a linear fitting coefficient R^2 of around 0.85 is convincing for the theoretical prediction of the molecular laser properties. The S_1 emission cross-sections and various absorption cross-sections near the emission wavelength (±125 nm) are

Table 1 The oscillator strength, theoretical photophysical properties and computational and experimental PLQY for twelve laser molecules

Molecule	f_{em}	k_r^S ($\times 10^8$ s^{-1})	k_{isc}^S (s^{-1})	k_{ic}^S ($\times 10^8$ s^{-1})	τ_{S_1} (ns)	τ_{T_1}[a] (ms)	Cal. PLQY[b]/Exp. PLQY (%)
***o*MDSB**	1.914	5.6	1.5×10^3	0.46	1.7	—	92/88
***p*MDSB**	2.153	6.7	9.9×10^2	0.96	1.3	—	87/87–91
βDCS	1.690	4.0	1.2×10^4	2.0	1.7	—	67/n.a.[c]
βDBDCS	1.878	3.4	6.6×10^3	0.42	2.7	—	89/84
βPDCS	1.343	3.3	7.2×10^6	0.46	2.6	—	86/95
BP3T	2.535	4.3	2.2×10^6	2.3	1.5	0.025	63/80
TPD	0.885	2.9	1.6×10^6	3.7	1.5	3.7	43/39–43
CzPSBF	1.601	5.1	6.4×10^6	6.2	0.88	0.12	45/55
CzPVSBF	2.802	6.3	2.7×10^5	3.8	0.99	0.051	63/40–44
TPASBF	1.873	4.6	5.3×10^5	6.1	0.93	0.069	43/46
TSBF	2.276	7.1	2.7×10^5	5.8	1.3	1.0	92/70–74
BSBCz	2.877	6.5	6.6×10^4	1.5	1.3	0.11	82/76

[a] τ_{T_1} is evaluated at SOC > 0.05 cm^{-1} for T_1/S_0. [b] Theoretical PLQY is evaluated *via* $\Phi = k_r^S/(k_r^S + k_{isc}^S + k_{ic}^S)$. [c] n.a. = not available.

estimated. Three molecules, **BP3T**, **CzPVSBF**, and **BSBCz**, outperform other systems, as their self-absorption and different species absorption cross-sections have little influence on the S_1 emission cross-sections, as shown in Fig. 4(b). As displayed in Tables 1 and 2, these three molecules also have a large electrical pumping net emission cross-section $\sigma_{em}^{net,ele}$, marginal intersystem crossing process (smaller k_{isc}^S than k_r^S), and short triplet lifetime τ_{T_1}. Therefore, **BP3T**, **CzPVSBF**, and **BSBCz** are prospective electrically pumped laser molecules. As a matter of fact, a narrow band emission has been observed from **BSBCz** upon being electrically pumped,[102] which clearly verifies the reliability of the screening scheme for the electrical pumping organic laser materials proposed in ref. 78. The computational screening protocol for organic small molecules used as lasers is summarized in Fig. 5(a).

3.3 Application of the laser screening protocol in TADF and MR-TADF molecules

Based on the screen-out protocol reported by Ou *et al.*, Lin *et al.* computationally researched a series of organic TADF and MR-TADF molecules for organic electrical pumping laser materials.[82] The 21 investigated molecules, including sixteen MR-TADF molecules[124,125] and five conventional TADF molecules,[126–128] are shown in Fig. 6(a) and (b), respectively. The structure optimization and excitation energies calculation were performed by B3LYP/6-31G(d) for MR-TADF molecules and ωB97XD/6-31G(d)//CAM-B3LYP/6-31G(d) (CAM-B3LYP for geometry optimized and ωB97XD for electronic energies) for conventional TADF molecules, respectively. SCS-CC2 was applied to evaluate the ΔE_{ST} for MR-TADF molecules in TURBOMOLE 7.4.[129] The photophysical rate constants were calculated using MOMAP[63–65] and show excellent consistency with experimental values, with the MAE value of around 7% for PLQY.

Four molecules, **ADBNA-Me-MesCz**, **2CzPN**, **4CzPN**, and **5CzBN**, with an oscillator strength of less than 0.1 are excluded. According to the proportional relationship between the threshold power and $1/(\sigma_{em}^{net,opt}\tau_{S_1})$, eight molecules with smaller $1/(\sigma_{em}^{net,opt}\tau_{S_1})$ values are selected as laser candidates and their photophysical properties are further analyzed. The explicit numbers of the oscillator strength, $1/(\sigma_{em}^{net,opt}\tau_{S_1})$ and photophysical parameters are listed in Table 3. A larger k_{risc}^T (compared to k_{nr}^T) can effectively promote the singlet harvesting process and establish the four-energy level. **D*t*BuPhCzB** and **ADBNA-Me-MesF** are further excluded because their k_{nr}^T is larger than k_{risc}^T. Through examining the electrical pumping net emission cross-section $\sigma_{eff}^{net,ele}$, which is given by the S_1 emission cross-sections and various absorption cross-sections, **D*t*BuCzB** is excluded due to severe self-absorption from $S_0 \rightarrow S_1$.[82] Finally, **4CzTPN** with negative $\sigma_{eff}^{net,ele}$ is also excluded and four molecules, **DABNA-2**, ***m*-Cz-BNCz**, **ADBNA-Me-Mes** and **ADBNA-Me-Tips**, are chosen as prospective candidates for electrical pumping laser materials. All eight molecules included in Table 3 can be used as optically

Table 2 The emission cross-sections and different absorption cross-sections for twelve laser molecules[a]

Molecule	σ_{em}	$\sigma_{abs}^{S_0 \rightarrow S_1}$	$\sigma_{abs}^{S_1 \rightarrow S_n}$	$\sigma_{abs}^{T_1 \rightarrow T_n}$	$\sigma_{abs}^{D_0^+ \rightarrow D_n^+}$	$\sigma_{abs}^{D_0^- \rightarrow D_n^-}$	$\sigma_{em}^{net,opt}$	$\sigma_{em}^{net,ele}$
***o*MDSB**	2.67	0.26	0.10	0.25	0.48	0.49	2.31	1.09
***p*MDSB**	3.00	0.65	0.11	0.21	0.47	0.56	2.24	1.00
βDCS	2.31	0.22	0.06	0.54	0.42	0.86	2.03	0.21
βDBDCS	2.76	0.31	0.10	0.33	0.28	1.39	2.35	0.35
βPDCS	1.75	0.05	0.10	0.00	0.39	0.51	1.60	0.75
BP3T	4.49	0.04	0.00	0.18	0.76	0.30	4.45	3.21
TPD	1.22	0.20	0.05	0.14	0.62	0.61	0.97	NA[b]
CzPSBF	2.20	0.25	0.00	0.06	0.36	1.00	1.95	0.53
CzPVSBF	5.30	0.72	0.00	0.24	0.56	1.15	4.58	2.63
TPASBF	2.90	0.30	0.05	0.12	0.70	1.23	2.55	0.50
TSBF	3.22	0.22	0.00	0.02	0.66	0.65	3.00	1.67
BSBCz	5.34	0.25	0.00	0.19	0.61	1.24	5.09	3.05

[a] Numbers are displayed in units of 10^{-16} cm^2. [b] The calculated value is negative.

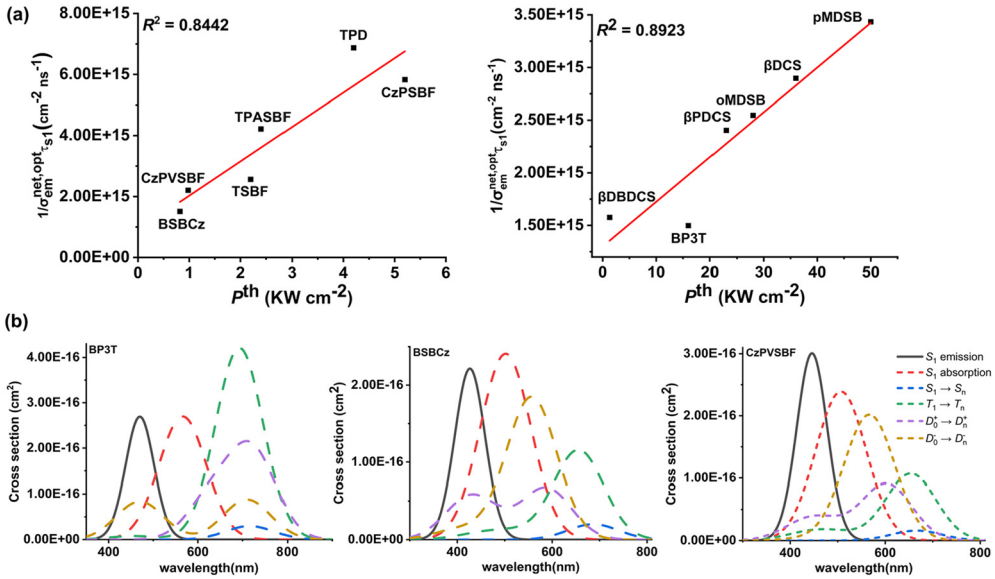

Fig. 4 The linear relationship between the experimental threshold power P^{th} and the product of the computed optical pumping net emission cross-section and the singlet lifetimes of the laser molecules and theoretically predicted S_1 emission cross-sections and various adjacent absorption cross-sections of the three candidate molecules for the electrically pumped laser. (a) The single crystal materials and thin film materials are shown in the left and right panels, respectively. (b) The black solid line and red dashed line correspond to the stimulated emission cross-section and self-absorption cross-section of S_1, respectively. Varied absorption cross-sections introduced by $S_1 \rightarrow S_n$ (blue dashed), $T_1 \rightarrow T_n$ (green dashed), $D_0^+ \rightarrow D_n^+$ (lavender dashed) and $D_0^- \rightarrow D_n^-$ (khaki dashed) are plotted around the emission wavelength (±125 nm). Due to insufficient space, the corresponding legends are only shown in **CzPVSBF** in Fig. 4(b) and the legends of **BP3T** and **BSBCz** are the same as that for **CzPVSBF**. (a) and (b) are reproduced with permission from ref. 78. Copyright 2020 Springer Nature.

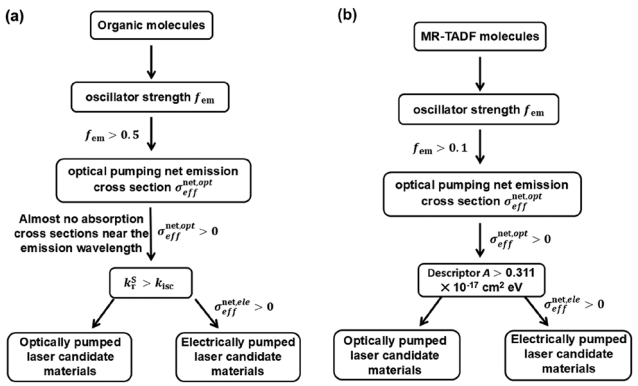

Fig. 5 Schematic of the theoretical prediction and screen of organic lasing molecules. (a) Theoretical calculation and screening scheme for organic laser molecules, validated based on experimental data. (b) Computational screening strategy for MR-TADF molecules as laser candidates.

pumped laser candidate molecules. In fact, the lasing behaviors of **DABNA-2**[130] and **4CzTPN**[131] have been experimentally validated, indicating that the laser screening strategy developed for organic fluorescent molecules is also applicable to TADF molecules.

3.4 Theoretical descriptor for quick screening of the MR-TADF laser candidate molecules with the DABNA and ADBNA skeletons

Li and Shuai proposed a molecular descriptor A for quickly screening the organic MR-TADF laser candidate materials.[132] The descriptor A is empirically derived by fitting the laser property parameters of four candidate laser molecules and the value range of A is plotted in Fig. 7. Descriptor A combines the singlet–triplet energy gap (ΔE_{ST}) and the net stimulated emission cross-section ($\sigma_{em}^{net,opt}$), both critical for laser performance. A small ΔE_{ST} promotes efficient RISC, while a large $\sigma_{em}^{net,opt}$ enhances light amplification. The product of these two parameters provides a balanced metric for the rapid screening of MR-TADF laser candidates without requiring full photophysical rate calculations. Four laser candidate molecules, DABNA-2, ADBNA-Me-Mes, ADBNA-Me-Tip and ADBNA-Me-MesF (Fig. 6(a)), have similar geometric configurations. Furthermore, the product of the singlet–triplet energy gap ΔE_{ST} and the optical pumping net stimulated emission cross-section $\sigma_{em}^{net,opt}$ is stable at around 0.490×10^{-17} cm^2 eV. Generally, a smaller ΔE_{ST} value can promote the RISC process of MR-TADF molecules, thereby facilitating the formation of a laser four-energy level system. A large emission cross-section $\sigma_{em}^{net,opt}$ is also undoubtedly beneficial for laser emission. Both ΔE_{ST} and $\sigma_{em}^{net,opt}$ are significant parameters for MR-TADF laser molecules. Therefore, descriptor A is defined to help determine whether the MR-TADF molecule can be used as a potential laser material. The $\sigma_{em}^{net,opt}$ is allowed to fluctuate within $\pm 1 \times 10^{-17}$ cm^2 due to experimental measurement error of the emission cross-section. Accordingly, the value of A lies within 0.311 to 0.670×10^{-17} cm^2 eV. The decreasing space of ΔE_{ST} for the MR-TADF molecules is small and a large $\sigma_{em}^{net,opt}$ is beneficial for light amplification. As a consequence, the range of A for MR-TADF molecules with the DABNA and ADBNA skeleton should be larger than 0.311×10^{-17} cm^2 eV. Although the value of the descriptor A

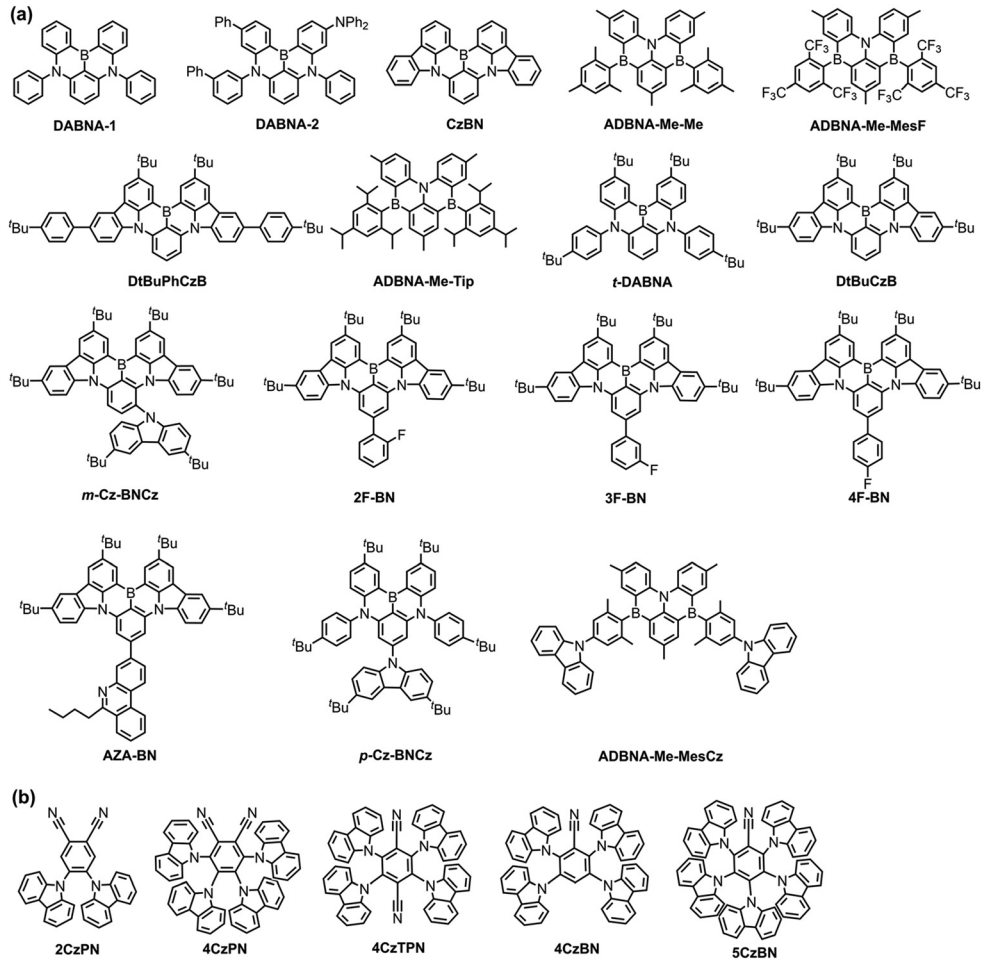

Fig. 6 The molecular structures of the investigated TADF and MR-TADF molecules. (a) The MR-TADF molecular structures. (b) The TADF molecular structures. (a) and (b) are reproduced with permission from ref. 82. Copyright 2022 American Chemical Society.

Table 3 The oscillator strength, laser properties and photophysical parameters for eight laser candidate molecules

Molecule	f_{em}	$1/(\sigma_{em}^{net,opt}\tau_{S_1})$ ($\times 10^{15}$ cm^{-2} ns^{-1})	k_r^S ($\times 10^8$ s^{-1})	k_{nr}^T ($\times 10^4$ s^{-1})	k_{risc}^T (s^{-1})	$\sigma_{em}^{net,opt}$ ($\times 10^{-17}$ cm^2)	$\sigma_{em}^{net,ele}$ ($\times 10^{-17}$ cm^2)
DABNA-2	0.242	3.706	0.702	9.61×10^3	9.19×10^5	2.194	1.258
***m*-Cz-BNCz**	0.155	3.325	0.352	7.87×10^3	4.10×10^5	1.460	1.215
D*t*BuCzB	0.355	7.298	1.01	5.71×10^1	1.97×10^4	1.584	0.501
D*t*BuPhCzB	0.503	6.375	1.36	7.79×10^3	6.64×10^3	2.366	2.358
ADBNA-Me-Mes	0.167	2.185	0.455	3.12×10^4	8.34×10^4	2.842	2.114
ADBNA-Me-Tip	0.173	1.966	0.430	3.10×10^4	3.33×10^4	3.064	2.648
ADBNA-Me-MesF	0.150	1.761	0.360	3.04×10^4	1.20×10^4	3.005	2.728
4CzTPN	0.116	7.469	0.251	5.16×10^{-3}	5.96×10^6	0.523	NA[a]

[a] The calculated value is negative.

is derived from empirical fitting, it is conveniently calculated through fundamental excited-state properties, oscillator strength, and emission energy, eliminating the need to evaluate various photophysical rate constants and emission/absorption cross-section curves, enabling the rapid screening of laser candidate molecules.

The lasing characteristics of 119 virtually designed MR-TADF molecules (Fig. 8(a) and (b)) are computationally explored through descriptor A, with the net emission cross-section of S_1 obtained *via* the screening scheme reported by Ou *et al.*[78] The geometry optimization and frequency analysis are calculated using B3LYP-D3/6-31G(d) based on the benchmark calculation by Lin *et al.*[82] Applying SCS-CC2 to calculate the ΔE_{ST} for a large number of MR-TADF molecules is too expensive. It is well known that the excitation energy calculation directly depends on the HF component. The higher the HF component, the higher the excitation energy calculated by the hybrid functional. Seven different density functions with different percentages of

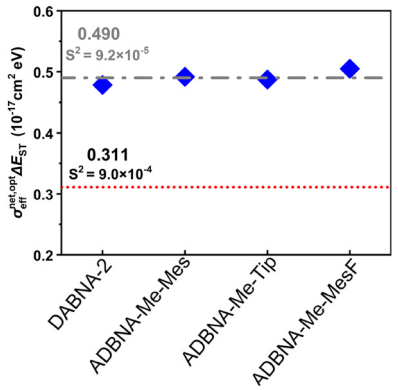

Fig. 7 The value range of descriptor *A* for the **DABNA**-type and **ADBNA**-type MR-TADF molecules. The gray dot-dashed line is a fitting line from the explicit numbers of four molecules. The red dotted line is the minimum value of descriptor *A*. S^2 represents the variance, and its unit is 10^{-34} cm^2 eV. Reproduced with permission from ref. 132. Copyright 2024 Elsevier B.V.

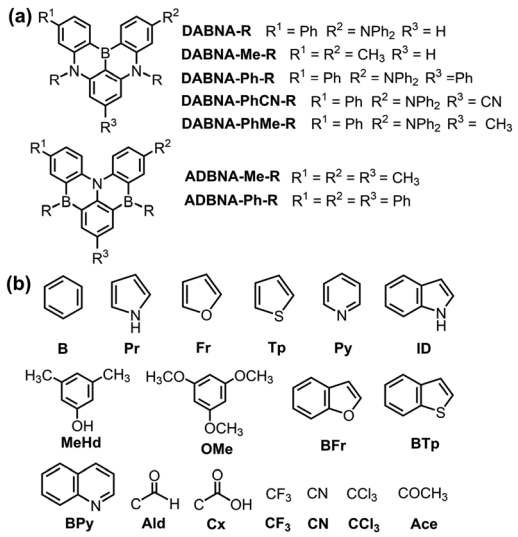

Fig. 8 (a) The body structures of the designed MR-TADF molecules. (b) The substituent structures *R* of the designed MR-TADF molecules. (a) and (b) are reproduced with permission from ref. 132. Copyright 2024 Elsevier B.V.

Hartree–Fock exact exchange, including TPSSh (10% HF),[133] PBE38 (37.5% HF),[134] PBE0-1/3 (33.33% HF),[135] PW6B95 (28% HF),[136] PBE0 (25% HF), BMK (42% HF)[137] and B3LYP-D3 (20% HF), are attempted to find two functionals with consistent predicted errors for S_1 and T_1 excitation energy. The double excitation property of MR-TADF molecules makes the ΔE_{ST} evaluation very sensitive to computational methods.[138] Therefore, **DABNA** and **ADBNA** derivative molecules in the benchmark calculation of ΔE_{ST} are independently considered. The excited energies of the singlet and triplet for **DABNA** derivatives are acquired by TD-B3LYP-D3/def2-TZVP and TD-BMK/def2-TZVP, respectively, with a MAE value of 0.038 eV compared with experimental values. The excited energies of the singlet and triplet states for the **ADBNA** derivatives are acquired by TD-TPSSh/def2-TZVP and TD-PBE38/def2-TZVP, respectively, with the MAE value smaller than 0.025 eV compared with experiments. The geometry optimization and excitation energy calculation are performed in Gaussian 16 and the photophysical rate constants are performed in MOMAP.

The oscillator strength, descriptor *A*, photophysical and laser parameters are listed in Table 4. Referring to the oscillator strength of the experimentally reported MR-TADF molecules, 36 molecules with a f_{em} of less than 0.1 are excluded. Then, descriptor *A* screened out 109 unreasonable MR-TADF molecules. Although the *A* value of **DABNA-PhCN-Fr** is 0.304×10^{-17} (which is less than 0.311×10^{-17} cm^2 eV), this discrepancy could potentially be due to calculation errors in ΔE_{ST}. Additionally, a large optical pumping emission cross-section is included in the further screening. Eight molecules, **DABNA-PhCN-B**, **DABNA-PhCN-BFr**, **DABNA-PhCN-BTp**, **DABNA-PhCN-ID**, **DABNA-PhCN-MeHd**, **DABNA-PhCN-Tp**, **DABNA-PhCN-Fr** and **ADBNA-Me-BPy**, are selected as optically pumped laser candidate materials. Further analysis reveals that these eight molecules exhibit large rate constants k_r^S and k_{risc}^T, and a small overlap in their emission/absorption cross-section curves, thereby validating the reliability of using descriptor *A* for quick screening. **ADBNA-Me-BPy** with a large k_r^S of 1.90×10^6 s^{-1} and k_{risc}^T of 1.01×10^8 s^{-1}, implying a low threshold power, is promising as an electrically pumped laser candidate molecule. Fig. 5(b) summarizes the computational strategy for screening MR-TADF molecules as laser candidates using descriptor *A*. The laser screening strategy for MR-TADF molecules proposed in this work can effectively promote the discovery of novel laser materials.

4. Organic phosphorescent materials

Metal complexes such as platinum and iridium are widely used in second-generation phosphorescent OLED materials due to

Table 4 The oscillator strength, descriptor *A*, photophysical parameters and laser properties for eight MR-TADF laser candidate molecules

Molecule	f_{em}	A ($\times 10^{-17}$ cm^2 eV)	k_r^S (s^{-1})	k_{risc}^T (s^{-1})	ΔE_{ST} (eV)	$\sigma_{em}^{net,opt}$ ($\times 10^{-17}$ cm^2)	$\sigma_{em}^{net,ele}$ ($\times 10^{-17}$ cm^2)
DABNA-PhCN-B	0.134	0.331	1.55×10^5	1.19×10^5	0.245	1.350	0.090
DABNA-PhCN-BFr	0.156	0.414	3.56×10^4	1.97×10^4	0.258	1.605	0.517
DABNA-PhCN-BTp	0.159	0.410	3.29×10^4	9.85×10^3	0.252	1.624	0.919
DABNA-PhCN-ID	0.487	0.377	5.27×10^7	8.05×10^7	0.268	1.406	NA[a]
DABNA-PhCN-MeHd	0.151	0.367	2.00×10^5	1.97×10^5	0.240	1.528	0.298
DABNA-PhCN-Tp	0.118	0.331	8.96×10^4	5.27×10^4	0.228	1.451	0.070
DABNA-PhCN-Fr	0.112	0.304	1.19×10^5	1.03×10^5	0.214	1.423	0.402
ADBNA-Me-BPy	0.127	0.503	1.90×10^6	1.01×10^8	0.248	2.029	1.320

[a] The calculated value is negative.

their breakthrough in overcoming low IQE. The structural relaxation from the triplet excited state to the ground state makes it difficult for these organometallic complexes to simultaneously achieve blue light emission and high color purity. In this section, we present the systematic theoretical elucidation of structure–property relationships and the efficient screening and design strategy for platinum(II)[138] and iridium(III)[139] complexes, providing useful guidance for the development of new molecules with superior photophysical properties.

4.1 Phosphorescence emission energy and spectrum.

Fig. 9 displays the potential energy surface diagram involving phosphorescence emission. In Fig. 9, the ground state energy E_g and triplet excited state energy $E_{t,u}$ can be calculated by DFT and UDFT methods, respectively.[140,141] $E_{t,td}$ and E_{gt} can be obtained by TD-DFT and singlet DFT single point energy calculation based on the T_1 optimized structure, respectively. According to Fig. 9, all four different phosphorescence emission energies, vertical excitation energies, $E_{v,td}$ and $E_{v,u}$, and adiabatic excitation energies, $E_{ad,td}$ and $E_{ad,u}$, computed using the TD-DFT and UDFT methods, respectively, can be obtained.

Fourteen density functionals with different percentages of HF component, including nine hybrid functionals B3LYP (20% HF), MN15 (44% HF),[142] M06-2X (54% HF), TPSSh (10% HF), BMK (42% HF), BHHLYP (50% HF),[143] B3LYP* (15% HF),[144] PBE0 (25% HF), PBE38 (37.5% HF), two range-separated hybrid functional ωB97X-D (short-range: 22.2% HF, long-range: 100% HF) and CAM-B3LYP (short-range: 19% HF, long-range: 65% HF), and three pure GGA functional PBE,[145] TPSS,[146] and BP86,[147,148] are used to benchmark the emission energies of 50 platinum(II) complexes in ref. 138. The molecular structures of 50 tetradentate platinum(II) complexes[149–166] are shown in Fig. 10. The calculated results of all 14 functionals indicate that $E_{v,td}$ yields the lowest values and $E_{ad,u}$ yields the highest values among the four different emission energies. The magnitudes of the $E_{ad,td}$ and $E_{v,u}$ values are varied by functionals. Computational results indicate that the predicted emission energy qualitatively increases with the increase of the HF component. Compared with experiments, among the four data sets by all functionals, B3LYP*/$E_{ad,u}$ performed the best, followed by B3LYP/$E_{ad,u}$ and MN15/$E_{v,u}$, which both achieved an AVR (average) within ±0.05 eV and RMSD (root mean squared error) of less than 0.10 eV. The predicted emission wavelength with respect to the experimental values reveals the accuracy of the qualitative predictions. The linear fitting coefficient R^2 of five functionals TPSSh, TPSS, PBE, B3LYP* and BP86 exceed 0.92, exhibiting a high degree of linearity. Grotjahn *et al.*[167] reported that based on the calculations of the phosphorescent emission energies of five tris(2,2′-bipyridine)-metal complexes ($[M(bpy)_3]^{n+}$, where M = Zn, Ru, Rh, Os, and Ir), the B3PW91 (20% HF)[168] functional gave an error of 0.09 eV by UDFT. Furthermore, the local hybrid functional LH12ct-SsirPW92[169] achieved a smaller MAE of 0.06 eV. Overall, B3LYP* is the most suitable functional for calculating phosphorescent emission energies.

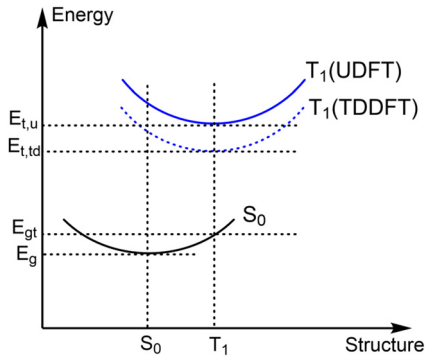

Fig. 9 The schematic of the potential energy surface. Reproduced with permission from ref. 138. Copyright 2025 the American Chemical Society.

In ref. 138, the vibrationally resolved emission spectra of each functional for 50 molecules in the T_1 state were calculated by MOMAP, and their shapes were compared with those obtained experimentally. Fig. 11 shows the calculated and experimental emission spectral shapes for molecule **PtOO7-dtb**. Four functionals, TPSSh, TPSS, PBE and BP86, always perform well especially for molecules with full width at half-maximum (FWHM) values of less than 30 nm and are highly consistent with the experimental spectra, with only the relative intensity of the shoulder peaks being different. Unfortunately, each functional provides some unphysical spectra for certain molecules (such as severe oscillations and/or abnormally broad FWHM). For example, BMK, PBE38, and MN15 for **PtOO7-dtb** even produced incorrect spectra that obviously violated physical laws, indicating that the results of the electronic structure calculations are problematic. M06-2X and MN15 generated more than 10 problematic spectra. The number of unphysical spectra given by TPSSh, TPSS, BP86, PBE and B3LYP* is less than 5 for all molecules. Therefore, TPSSh, TPSS, BP86, PBE and B3LYP* are reliable functionals with a satisfactory robustness for calculating the phosphorescence emission spectrum.

The influence of the internal coordinates and Cartesian coordinates is explored with the TPSSh functional. The emission spectra are computed with the electron-vibronic coupling results given by both internal and Cartesian coordinates. For most molecules, particularly molecules with a narrowband emission, the spectral shapes obtained from the two coordinate systems exhibit very little differences, as shown by Fig. 12. The application of Cartesian coordinates for flexible molecule **PtON1-Ph** provides a very wide spectrum, while the result from the internal coordinates is reasonably narrow. The Duschinsky rotation effect (DRE) to the emission spectra is also accessed, which has a very minor effect on the spectra of most molecules, as shown in Fig. 12. Although the effect of the coordinate and DRE on the phosphorescence spectrum is small, it is still recommended to prioritize using internal coordinates with DRE.

4.2 The structure–property relationship of platinum(II) complexes

Chen *et al.* also investigated the charge density difference (CDD) and vibrational properties to obtain the structure–property relationship and identify the key factors determining color

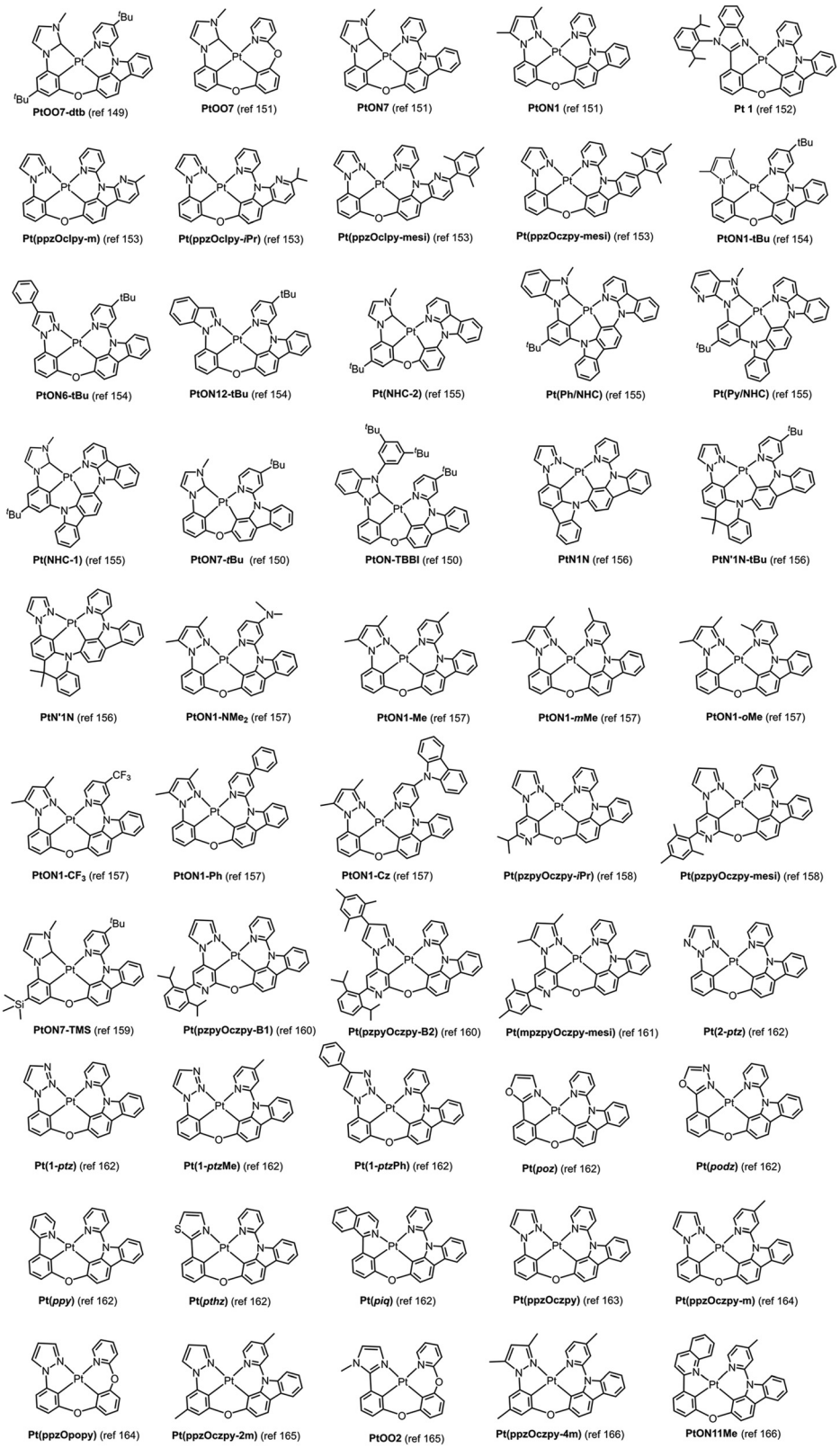

Fig. 10 The chemical structures of the tetradentate platinum(II) complexes. Reproduced with permission from ref. 138. Copyright 2025 the American Chemical Society.

purity.[138] Fig. 13 shows the reorganization energy distribution, the two vibrational modes with the largest reorganization energy, and the CDD diagram for the narrowband molecule **PtOO7-dtb** and broadband molecule **Pt(Py/NHC)**, respectively.

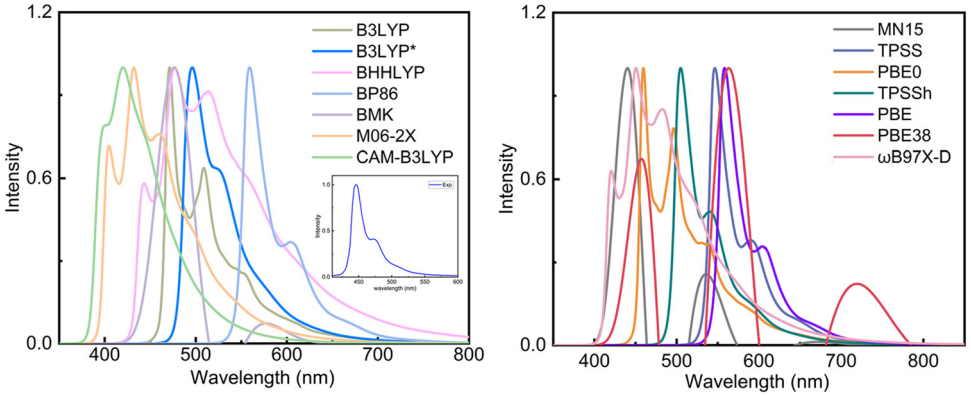

Fig. 11 The 14 different functionals calculated emission spectra and experimental emission spectra of **PtOO7-dtb**. Reproduced with permission from ref. 138. Copyright 2025 the American Chemical Society.

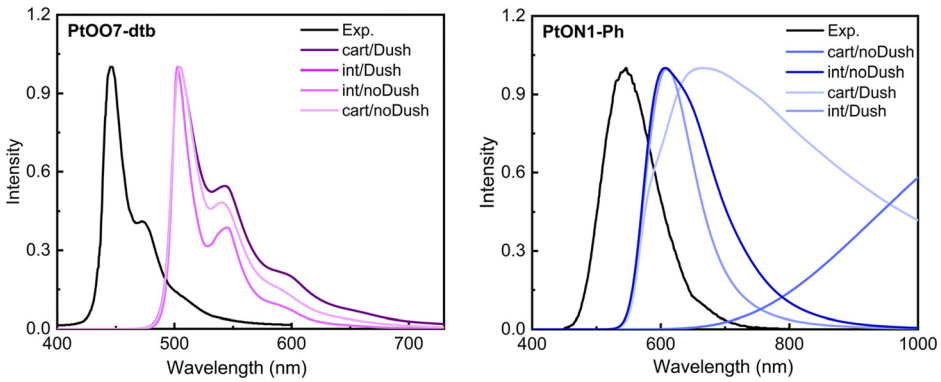

Fig. 12 The TPSSh-calculated spectra with the Cartesian and internal coordinates, with or without the Duschinsky rotation effect for molecules **PtOO7-dtb** and **PtON1-Ph**. The spectra with the Cartesian coordinate and no DRE are overlapped with that of the internal coordinate with DRE in the left panel. Reproduced with permission from ref. 138. Copyright 2025 the American Chemical Society.

The regions of electronic density change are highly consistent with the two predominant vibrational modes for the narrow-band molecule, indicating that the two vibrational modes lead to the shoulder peaks and the remaining vibrational modes contribute minimally to the reorganization energy, which results in a very narrow main peak in the spectrum. For broadband molecules, although electrons are still mainly transferred from the platinum center and the carbazole moiety, the conjugation of the pyridine ring with other structures increases the electron-accepting region, which activates the low-

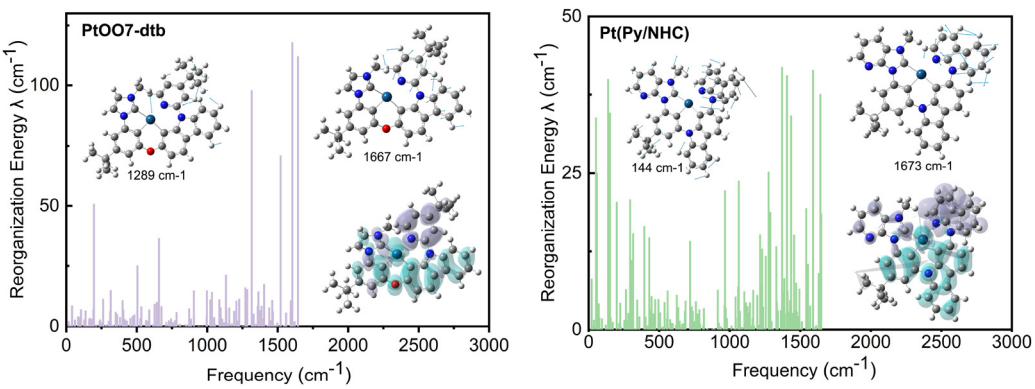

Fig. 13 The reorganization energy distribution along different vibrational frequencies, the two vibrational modes with the largest reorganization energies and CDD plots for **PtOO7-dtb** (left panel) and **Pt(Py/NHC)** (right panel), respectively. The purple and green surfaces represent the increasing and decreasing charge density from the S_0-to-T_1 transition. Reproduced with permission from ref. 138. Copyright 2025 the American Chemical Society.

frequency modes and suppresses the vibrational mode near 1290 cm^{-1}. Therefore, the key factor for achieving the high color purity of these tetradentate Pt(II) molecules is the presence of a pyridine–carbazole–oxygen moiety and the non-conjugation of pyridine groups with other structures.

4.3 Automatic screen-out strategy of iridium(III) complexes

In ref. 139, a HTVS process is applied to automatically screen out Ir(III) complexes as promising phosphorescent emitters. The overall HTVS workflow is shown in Fig. 14. 278 bidentate ligands are collected based on Ir(III) complexes[170] previously reported experimentally, and a million molecules are constructed using stk.[171] By filtering out unphysical structures based on atomic distances and/or ligand angles, approximately 1.6 million candidate molecules are subsequently optimized using the density functional tight-binding method GFN2-xTB.[172] In the pre-training process of Uni-Mol, coordinates and symbols are used as initial guesses for QM computation and self-learning labels, while the HOMO and LUMO energies at the GFN2-xTB level are used as supervise-learning labels. A total of 1468 molecules with less than 61 heavy atoms are randomly selected from the candidate pool for QM calculations. The fine-tuning of the pre-trained model makes use of the four QM predictions, HOMO, LUMO, adiabatic excitation energy of T_1 (E_{ad}) and photoluminescence quantum yield (PLQY). All electronic structure calculations are performed using quantum chemistry packages Gaussian16[66] and ORCA.[67] PLQY is evaluated by the MOMAP program.

The structural optimization of the ground state and the T_1 state is based on DFT and UDFT using B3LYP combined with the 6-31G** basis set for nonmetal atoms and the LANDL2DZ[173,174] effective core potential for the Ir atom, respectively. The E_{ad} are calculated at the T_1 optimized structure by TD-DFT with TDA and PBE0-1/3 functionals. The B3LYP functional and DKH-def2-TZVP basis set are applied to evaluate the SOC between T_1 and S_0, and the transition dipole moment (TDM) of T_1.[175] The E_{ad} and PLQY of experimentally reported molecules are shown in Table 5. Comparing the theoretically predicted values and experimental values of E_{ad} and PLQY of ten experimental molecules[176–185] verifies the accuracy of the QM calculation. It indicates that the PBE0-1/3 functional and TVCF allows for the reasonable prediction of phosphorescent emission energies and PLQYs in iridium complexes.

The performances of Uni-mol on the Ir(III) complexes pool are tested. The pre-training process uses the energy of the frontier orbitals at the GFN2-xTB level as labels, with a partitioning ratio of 8 : 1 : 1. The *R* values of HOMO and LUMO on the test set are 0.995 and 0.934, respectively, indicating consistency between the Uni-Mol prediction and GFN2-xTB calculation. The fine-tuning based on the E_{ad}, HOMO, LUMO, and PLQY, also has the same division ratio. The correlation coefficient and MAE between Uni-mol and QM calculation are shown in Fig. 15. HOMO, LUMO and E_{ad} all have good prediction accuracy with MAEs of 0.067, 0.114 and 0.043, and *R* values of 0.95, 0.87 and 0.96, respectively. The accuracy of the predicted PLQY is relatively poor. This is because the calculation of PLQY not only relies on pure electronic structural properties, but also requires the calculation of radiative and non-radiative decay rate constants through rate formalization. That being said, with an MAE of 9.4%, Uni-Mol can serve as a rather reliable predictor for PLQY, which is computationally expensive *via* QM methods.

Fig. 16(a) shows the final screening strategy of the Ir(III) complex. Firstly, based on the predicted emission energy of all 1.6 million candidates by Uni-Mol, the red, yellow, green and blue emitters are selected. Then, the red and yellow molecules with a PLQY value greater than 40%, and the blue and green molecules with a PLQY value greater than 80%, are selected. Finally, by excluding the molecules with three different ligands and unreasonably large molecular weight, potential candidate molecules can be obtained. The search strategy recovers some well-known phosphorescent emitters, such as some $(dfppy)_2Ir(NHC)$ complexes[185] and $Ir(Fppy)_2(acac)$, FIrpic,[186] thereby verifying the rationality of the theoretical scheme. Fig. 16(b) and (c) show the emission spectra and structure of five candidate molecules, respectively. The filtered green emitter **89_89_228** and blue emitter **152_189_189** stand out, showing significantly narrower FWHM

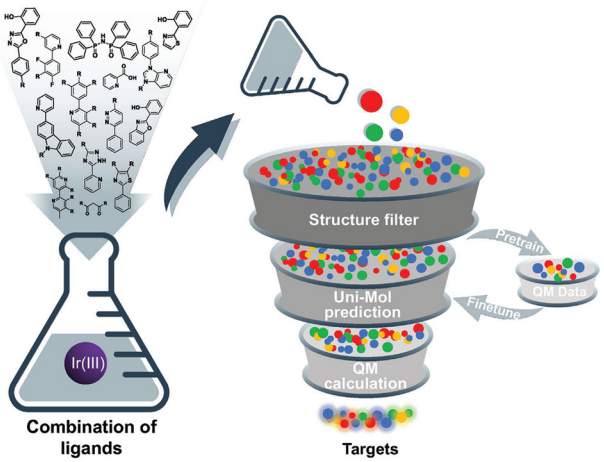

Fig. 14 Schematic of the HTVS workflow for Ir(III) complex emitters. Reproduced with permission from ref. 139. Copyright 2023 John Wiley and Sons, Inc.

Table 5 The PLQY and E_{ad} of the QM predicted and experimentally reported values for Ir(III) complexes

	PLQY		E_{ad} (eV)	
Molecule	QM	Exp.	QM	Exp.[a]
$(ppy)_2Ir(oz)$[176]	0.30	0.55	2.60	2.58
$Ir(dpt)_3$[177]	0.99	0.64	3.14	3.13
Complex **2**[178]	0.39	0.35	2.62	2.44
$(mdp)_2Ir(acac)$[179]	0.76	0.85	2.40	2.37
Complex **1**[180]	0.78	0.78	2.97	3.12
IrS-5F[181]	0.67	0.95	2.47	2.35
Ir 1[182]	0.99	0.93	2.46	2.75
2FBNO[183]	0.83	0.71	2.37	2.45
Complex **3**[184]	0.90	0.73	2.63	2.94
Ir5b[185]	0.99	0.69	2.91	2.96

[a] The values are estimated by the average of the absorption and emission energies.

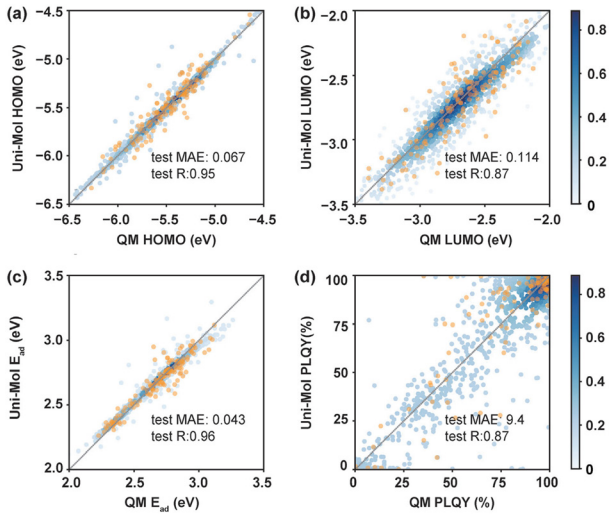

Fig. 15 The correlation coefficient and MAE between the Uni-mol predicted values and QM calculated values for the (a) HOMO, (b) LUMO, (c) E_{ad} and (d) PLQY. The blue and yellow dots represent the data from the training and testing sets, respectively. The color bars are the density of data points in the training set. Reproduced with permission from ref. 139. Copyright 2023 John Wiley and Sons, Inc.

values of 38 nm and 52 nm, respectively, compared to common green and blue phosphorescent emitters. The red emitter **41_41_75**, although having a slightly wider FWHM, exhibits a dominant emission peak at 611 nm, corresponding to a satisfactory CIE coordinate of (0.66, 0.34) for red emission. The predicted emission spectra of the sky-blue emitter **197_197_210** and the yellow-orange emitter **44_44_229** show main peaks at 474 nm and 574 nm, respectively, with both having FWHM values of greater than 85 nm. By adjusting the mixing ratio of these two colors, pure white emission with CIE coordinates (0.32, 0.33) can be achieved, as illustrated in the insets of Fig. 16(b). Thus, Uni-mol is a powerful tool for the rational and effective design and screening of luminescent molecules.

5. Summary and outlook

In conclusion, with the combination of the quantum chemistry calculation packages and the MOMAP program, the photophysical properties of a series of organic molecules, including normal fluorescent molecules, conventional TADF and MR-TADF molecules, as well as phosphorescent organometallic complexes, can be accurately predicted as evinced in the previously introduced literature. A reliable screening protocol for organic fluorescent molecules, TADF and MR-TADF molecules as optically and electronically pumped laser materials, and high-throughput virtual screening strategy for organic phosphorescent materials have been obtained based on a comprehensive computational protocol benchmarked with experiments. The theoretical progresses in organic luminescent molecules effectively accelerate the exploration of OLED materials, thus allowing the development of novel and high-efficiency organic display materials.

While significant advances have been made in both experimental and theoretical realms, considerable challenges remain to be addressed. First, the exploration of TADF and MR-TADF molecules for organic electroluminescence and light amplification is still in its early stages, with only a limited number of systems studied compared to the vast library of reported organic molecules. The potential of other molecular architectures—such as those containing NC═O or heavy-atom dopants like S/Se—for achieving narrowband emission remains largely unexplored. Second, the development of highly efficient deep-blue organometallic emitters continues to pose a major hurdle, largely due to the susceptibility of metal-centered d–d states to non-radiative decay. Pt(II) complexes with bidentate or

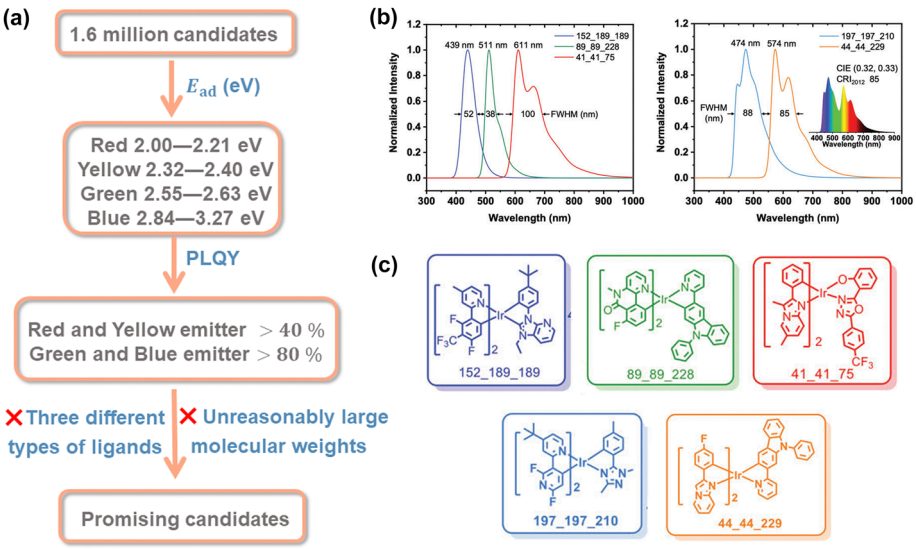

Fig. 16 (a) Schematic of the screening strategy for the Ir(III) complex. (b) The emission spectra, FWHM and (c) chemical structure of the predicted promising molecules. The different colored spectrum shapes in panel (b) correspond to the colored molecular structures in panel (c). (b) and (c) are reproduced with permission from ref. 139. Copyright 2023 John Wiley and Sons, Inc.

tridentate ligands, for instance, often suffer from low quantum yields or poor stability arising from geometric distortion or the use of monoanionic ligands. Third, in device settings, various absorption losses and efficiency roll-off phenomena critically limit the external quantum efficiency. Strategies to mitigate these optical losses are essential for improving device performance. Finally, from a theoretical standpoint, the high computational cost of benchmarking and selecting appropriate levels of theory remains a barrier. There is a clear need for developing more efficient and accurate methods capable of simulating complex photophysical processes—such as nonadiabatic transitions between excited states—to better guide material design. We hope that this overview of recent progress and prevailing challenges will stimulate further research and accelerate the development of high-performance organic luminescent materials.

Author contributions

All authors contributed to the conception, structuring, and writing of this review.

Conflicts of interest

There are no conflicts to declare.

Data availability

No primary research results, software or code have been included and no new data were generated or analysed as part of this review.

Acknowledgements

This work is supported by the Shenzhen Science and Technology Peacock Team Program (No. KQTD20240729102028011) and the National Natural Science Foundation of China (Grant No. T2350009 and 22433007), as well as the Guangdong Provincial Natural Science Foundation (Grant No. 2024A1515011185). Q. O. is supported by the research grants from China Petroleum & Chemical Corp. (Funding number 124014). R. L. and Z. S. are supported by the Guangdong Basic Research Center of Excellence for Aggregate Science.

Notes and references

1 A. VanSlyke, C. W. Tang and L. C. Roberts, (Eastman Kodak Co), USA US4720432A, 1987.
2 S. S. Swayamprabha, D. K. Dubey, Shahnawaz, R. A. K. Yadav, M. R. Nagar, A. Sharma, F. C. Tung and J. H. Jou, *Adv. Sci.*, 2021, **8**, 2002254.
3 M. A. McCarthy, B. Liu, E. P. Donoghue, I. Kravchenko, D. Y. Kim, F. So and A. G. Rinzler, *Science*, 2011, **332**, 570–573.
4 K. Jiang, X. Chang, J. Q. Zhu, T. Zhu, J. T. Yu, Y. F. Wang, Y. M. Zhang, D. G. Ma and W. G. Zhu, *Angew. Chem., Int. Ed.*, 2024, e202421520.
5 Q. Y. Meng, X. L. Wen and J. Qiao, *J. Phys. Chem. Lett.*, 2024, **15**, 12571–12583.
6 G. Hong, X. M. Gan, C. Leonhardt, Z. Zhang, J. Seibert, J. M. Busch and S. A. Bräse, *Adv. Mater.*, 2021, **33**, 2005630.
7 M. A. Baldo, D. F. O'brien, M. E. Thompson and S. R. Forrest, *Phys. Rev. B: Condens. Matter Mater. Phys.*, 1999, **60**, 14422–14428.
8 S. Abdullah, E. J. C. Dias, J. Krpensky, V. Mkhitaryan and F. J. G. D. Abajo, *ACS Photonics*, 2024, **11**, 2183–2193.
9 X. B. Shi, Y. Liu, Z. Yuan, X. K. Liu, Y. Miao, J. Wang, S. Lenk, S. Reineke and F. Gao, *Adv. Opt. Mater.*, 2018, **6**, 1800667.
10 P. V. Kolesnichenko, M. Hertzog, F. Hainer, O. Kefer, J. Zaumseil and T. Buckup, *ACS Photonics*, 2025, **12**, 3344–3354.
11 W. P. Liu, S. P. Xu, X. L. Yang, H. T. Hang, X. Y. Du, J. Xi, Y. S. Ding, G. J. Zhou, Z. Chen and Y. H. Sun, *Chem. Eng. J.*, 2025, **503**, 158284.
12 B. Xu, F. Meng, S. Zhu, Y. Li, L. Ji, C. Qiao, C. Zhang and J. Zhang, *Nano Lett.*, 2025, **25**, 11601–11608.
13 Z. Yang, M. Zhu, Z. Xie, Y. Zhang, S. Liu, J. Zhao, J. Xu, Z. Chi and M. P. Aldred, *Chem. Soc. Rev.*, 2017, **46**, 915–1016.
14 M. Mamada, M. Hayakawa, J. Ochi and T. Hatakeyama, *Chem. Soc. Rev.*, 2024, **53**, 1624.
15 X. Li, Y. Wang, Z. Zhang, S. Cai, Z. An and W. Huang, *Adv. Mater.*, 2023, **36**, 2308290.
16 P. Data and Y. Takeda, *Chem. – Asian J.*, 2023, **14**, 1613–1636.
17 Y. Li, M. Gecevicius and J. Qiu, *Chem. Soc. Rev.*, 2016, **45**, 2090.
18 C. Bilen, N. Harrison and D. Morantz, *Nature*, 1978, **271**, 235.
19 S. Fung, T. Zou, B. Cao, T. Chen, W. P. To, C. Yang, C. N. Lok and C. M. Che, *Nat. Commun.*, 2016, **7**, 10655.
20 Z. Q. Zhu, K. Klimes, S. Holloway and J. Li, *Adv. Mater.*, 2017, **29**, 5.
21 B. N. Li, Y. G. Li, M. H. Y. Chan and V. W. W. Yam, *J. Am. Chem. Soc.*, 2021, **143**, 21676–21684.
22 L. Wang, J. S. Miao, Y. M. Zhang, C. J. Wu, H. Huang, X. Z. Wang and C. L. Yang, *Adv. Mater.*, 2023, **35**, 9.
23 Z. Yang, Z. Mao, Z. Xie, Y. Zhang, S. Liu, J. Zhao, J. Xu, Z. Chi and M. P. Aldred, *Chem. Soc. Rev.*, 2017, **46**, 915.
24 M. Mamada, M. Hayakawa, J. Ochi and T. Hatakeyama, *Chem. Soc. Rev.*, 2024, **53**, 1624.
25 Y. Tao, K. Yuan, T. Chen, P. Xu, H. Li, R. Chen, C. Zheng, L. Zhang and W. Huang, *Adv. Mater.*, 2014, **26**, 7931–7958.
26 M. Zhang, C. J. Zheng, H. Lin and S. L. Tao, *Mater. Horiz.*, 2021, **8**, 401–425.
27 Y. F. Chang, Y. L. Wu, X. D. Wang, W. L. Li, Q. Q. Yang, S. M. Wang, S. Y. Shao and L. X. Wang, *Chem. Eng. J.*, 2023, **451**, 138545.
28 J. Li, Z. Li, H. Liu, H. Q. Gong, J. C. Zhang and Q. Guo, *Front. Chem.*, 2022, **10**, 952116.
29 J. J. Hu, X. F. Luo, Y. P. Zhang, M. X. Mao, H. X. Ni, X. Liang and Y. X. Zheng, *J. Mater. Chem. C*, 2022, **10**, 768–773.

30 D. D. Zhang, X. Z. Song, M. H. Cai, H. Kaji and L. Duan, *Adv. Mater.*, 2018, **30**, 1705406.
31 B. W. Lei, Z. M. Huang, S. T. Li, J. J. Liu, Z. Y. Bin and J. S. You, *Angew. Chem., Int. Ed.*, 2023, **62**, e202218405.
32 Y. Liu, X. Xiao, Y. Ran, Z. Y. Bin and J. S. You, *Chem. Sci.*, 2021, **12**, 9408–9412.
33 Y. W. Zhang, G. M. Li, L. Wang, T. Y. Huang, J. B. Wei, G. Y. Meng, X. Wang, X. Zeng, D. D. Zhang and L. Duan, *Angew. Chem., Int. Ed.*, 2022, **61**, e202202380.
34 M. Nagata, H. Min, E. Watanabe, H. Fukumoto, Y. Mizuhata, N. Tokitoh, T. Agou and T. Yasuda, *Angew. Chem., Int. Ed.*, 2021, **60**, 20280–20285.
35 I. S. Park, M. L. Yang, H. Shibata, N. Amanokura and T. Yasuda, *Adv. Mater.*, 2022, **34**, 2107951.
36 X. S. Cao, K. Pan, J. S. Miao, X. L. Lv, Z. Y. Huang, F. Ni, X. J. Yin, Y. X. Wei and C. L. Yang, *J. Am. Chem. Soc.*, 2022, **144**, 22976–22984.
37 H. Peng, Y. L. Xu, C. J. Zhou, R. R. Pei, J. S. Miao, H. Liu and C. L. Yang, *Adv. Funct. Mater.*, 2023, **33**, 2211696.
38 T. Hatakeyama, K. Shiren, K. Nakajima, S. Nomura, S. Nakatsuka, K. Kinoshita, J. P. Ni, Y. Ono and T. Ikuta, *Adv. Mater.*, 2016, **28**, 2777–2781.
39 H. Nakanotani, T. Higuchi, T. Furukawa, K. Masui, K. Morimoto, M. Numata, H. Tanaka, Y. Sagara, T. Yasuda and C. Adachi, *Nat. Commun.*, 2014, **5**, 4016.
40 D. Zhang, X. Song, M. Cai and L. Duan, *Adv. Mater.*, 2018, **30**, 1705250.
41 C. Y. Chan, M. Tanaka, Y. T. Lee, Y. W. Wong, H. Nakanotani, T. Hatakeyama and C. Adachi, *Nat. Photonics*, 2021, **15**, 203–207.
42 N. Haase, A. Danos, C. Pflumm, P. Stachelek, W. Brütting and A. P. Monkman, *Mater. Horiz.*, 2021, **8**, 1805–1815.
43 N. Aizawa, Y. J. Pu, Y. Harabuchi, A. Nihonyanagi, R. Ibuka, H. Inuzuka, B. Dhara, Y. Koyama, K. Nakayama, S. Maeda, F. Araoka and D. Miyajima, *Nature*, 2022, **609**, 502–506.
44 W. Leupin and J. Wirz, *J. Am. Chem. Soc.*, 1980, **102**, 6068–6075.
45 P. Silva, *J. Phys. Chem. Lett.*, 2019, **10**, 5674–5679.
46 D. Jacquemin, E. A. Perpète, O. A. Vydrov, G. E. Scuseria and C. Adamo, *J. Chem. Phys.*, 2007, **127**, 094102.
47 D. Jacquemin, V. Wathelet, E. A. Perpete and C. Adamo, *J. Chem. Theory Comput.*, 2009, **5**, 2420–2435.
48 F. Muniz-Miranda, A. Pedone, G. Battistelli, M. Montalti, J. Bloino and V. Barone, *J. Chem. Theory Comput.*, 2015, **11**, 5371–5384.
49 X. K. Chen, *CCS Chem.*, 2020, **2**, 1256–1267.
50 A. D. Laurent and D. Jacquemin, *Int. J. Quantum Chem.*, 2013, **113**, 2019–2039.
51 D. Jacquemin, E. A. Perpète, G. E. Scuseria, I. Ciofini and C. Adamo, *J. Chem. Theory Comput.*, 2008, **4**, 123–135.
52 D. Jacquemin, A. Planchat, C. Adamo and B. Mennucci, *J. Chem. Theory Comput.*, 2012, **8**, 2359–2372.
53 A. Pershin, D. Hall, V. Lemaur, J. C. Sancho–Garcia, L. Muccioli, E. Zysman-Colman, D. Beljonne and Y. Olivier, *Nat. Commun.*, 2019, **10**, 597.
54 K. Shizu and H. Kaji, *Nat. Commun.*, 2024, **15**, 4723.
55 D. Hall, J. C. Sancho-García, A. Pershin, G. Ricci, D. Beljonne, E. Zysman-Colman and Y. Olivier, *J. Chem. Theory Comput.*, 2022, **18**, 4903–4918.
56 A. Dreuw and M. Wormit, *Wiley Interdiscip. Rev.: Comput. Mol. Sci.*, 2015, **5**, 82–95.
57 S. Grimme, *J. Chem. Phys.*, 2003, **118**, 9095–9102.
58 T. Froitzheim, S. Grimme and J. M. Mewes, *J. Chem. Theory Comput.*, 2022, **18**, 7702–7713.
59 D. Hall, J. C. Sancho-García, A. Pershin, D. Beljonne, E. Zysman-Colman and Y. Olivier, *J. Phys. Chem. A*, 2023, **127**, 4743–4757.
60 M. Hempe, N. A. Kukhta, A. Danos, M. A. Fox, A. S. Batsanov, A. P. Monkman and M. R. Bryce, *Chem. Mater.*, 2021, **33**, 3066–3080.
61 I. Kim, K. H. Cho, S. O. Jeon, W. Son, D. Kim, Y. M. Rhee, I. Jang, H. Choi and D. S. Kim, *JACS Au*, 2021, **1**, 987–997.
62 I. Kim, S. O. Jeon, D. Jeong, H. Choi, W. Son, D. Kim, Y. M. Rhee and H. S. Lee, *J. Chem. Theory Comput.*, 2020, **16**, 621–632.
63 Q. Peng, Y. Yi, Z. Shuai and J. Shao, *J. Am. Chem. Soc.*, 2007, **129**, 9333–9339.
64 Z. Shuai, *Chin. J. Chem.*, 2020, **38**, 1223–1232.
65 Z. Shuai and Q. Peng, *Nat. Sci. Rev.*, 2017, **4**, 224–239.
66 M. J. Frisch, *et al.*, *Gaussian 16 Rev. C.01*, Gaussian, Inc., Wallingford CT, 2016.
67 F. Neese, *Wiley Interdiscip. Rev.: Comput. Mol. Sci.*, 2018, **8**, e1327.
68 Y. Shao, *et al.*, *Mol. Phys.*, 2015, **113**, 184–215.
69 G. Zhou, Z. Gao, Q. Ding, H. Zheng, H. Xu, Z. Wei, L. Zhang and G. Ke, *The Eleventh International Conference on Learning Representations*, 2023.
70 G. Q. Wei, X. D. Wang and L. S. Liao, *Adv. Funct. Mater.*, 2019, **29**, 1902981.
71 J. J. Wu, X. D. Wang and L. S. Liao, *ACS Photonics*, 2019, **6**, 2590–2599.
72 D. Jacquemin, V. Wathelet, E. A. Perpète and C. Adamo, *J. Chem. Theory Comput.*, 2009, **5**, 2420–2435.
73 A. D. Becke, *J. Chem. Phys.*, 1993, **98**, 5648–5652.
74 C. Adamo and V. Barone, *J. Chem. Phys.*, 1999, **110**, 6158–6170.
75 C. Adamo and V. Barone, *Chem. Phys. Lett.*, 1997, **274**, 242–250.
76 O. A. Vydrov, J. Heyd, V. Krukau and G. E. Scuseria, *J. Chem. Phys.*, 2006, **125**, 074106.
77 K. Gong, J. Yang, T. T. Testoff, W. Li, T. Wang, D. Liu, X. Zhou and L. Wang, *J. Chem. Phys.*, 2021, **549**, 111256.
78 Q. Ou, Q. Peng and Z. Shuai, *Nat. Commun.*, 2020, **11**, 4485.
79 X. Wu, X. Xie and A. Troisi, *J. Mater. Chem. C*, 2024, **12**, 18886–18892.
80 Y. Zhao and D. G. Truhlar, *Theor. Chem. Acc.*, 2008, **120**, 215–241.
81 H. Sun, C. Zhong and J. L. Bredas, *J. Chem. Theory Comput.*, 2015, **11**, 3851–3858.
82 S. Lin, Q. Ou and Z. Shuai, *ACS Mater. Lett.*, 2022, **4**, 487–496.
83 J. D. Chai and M. Head-Gordon, *Phys. Chem. Chem. Phys.*, 2008, **10**, 6615–6620.

84 D. Hall, J. C. Sancho-García, A. Pershin, D. Beljonne, E. Zysman-Colman and Y. Olivier, *J. Phys. Chem. A*, 2023, **127**, 4743–4757.
85 T. Yanai, D. P. Tew and N. C. Handy, *Chem. Phys. Lett.*, 2004, **393**, 51–57.
86 M. A. Rohrdanz, K. M. Martins and J. M. Herbert, *J. Chem. Phys.*, 2009, **130**, 054112.
87 Sanyam, R. Khatua and A. Monda, *J. Chem. Theory Comput.*, 2023, **19**, 9290–9301.
88 S. Grimme, *J. Chem. Phys.*, 2006, **124**, 034108.
89 R. Kabe, H. Nakanotani, T. Sakane, M. Yahiro and C. Adachi, *Adv. Mater.*, 2009, **21**, 4034–4038.
90 Y. Xu, H. Zhang, F. Li, F. Shen, H. Wang, X. Li, Y. Yu and Y. Ma, *J. Mater. Chem.*, 2012, **22**, 1592–1597.
91 S. Varghese, S. J. Yoon, S. Casado, R. C. Fischer, R. Wannemacher, S. Y. Park and J. Gierschner, *Adv. Opt. Mater.*, 2014, **2**, 542–548.
92 H. Wang, F. Li, I. Ravia, B. Gao, Y. Li, V. Medvedev, H. Sun, N. Tessler and Y. Ma, *Adv. Funct. Mater.*, 2011, **21**, 3770–3777.
93 M. Ichikawa, K. Nakamura, M. Inoue, H. Mishima, T. Haritani, R. Hibino, T. Koyama and Y. Taniguchi, *Appl. Phys. Lett.*, 2005, **87**, 221113.
94 Y. Kawamura, H. Yamamoto, K. Goushi, H. Sasabe, C. Adachi and H. Yoshizaki, *Appl. Phys. Lett.*, 2004, **84**, 2724–2726.
95 T. Komino, H. Nomura, M. Yahiro, K. Endo and C. Adachi, *J. Phys. Chem. C*, 2011, **115**, 19890–19896.
96 T. Oyamada, C. Chang, T. Chao, F. Fang, C. Wu, K. Wong, H. Sasabe and C. Adachi, *J. Phys. Chem. C*, 2007, **111**, 108–115.
97 B. Xu, H. Fang, Y. Dong, F. Chen, Q. Chen, H. Sun and W. Tian, *New J. Chem.*, 2010, **34**, 1838–1842.
98 H. Nakanotani, S. Akiyama, D. Ohnishi, M. Moriwake, M. Yahiro, T. Yoshihara, S. Tobita and C. Adachi, *Adv. Funct. Mater.*, 2007, **17**, 2328–2335.
99 Y. Xu, H. Zhang, F. Li, F. Shen, H. Wang, X. Li, Y. Yu and Y. Ma, *J. Mater. Chem.*, 2012, **22**, 1592–1597.
100 H. Nakanotani, M. Saito, H. Nakamura and C. Adachi, *Appl. Phys. Lett.*, 2009, **95**, 033308.
101 Z. Xie, H. Wang, F. Li, W. Xie, L. Liu, B. Yang, L. Ye and Y. Ma, *Cryst. Growth Des.*, 2007, **7**, 2512–2516.
102 A. S. D. Sandanayaka, K. Yoshida, M. Inoue, C. Qin, K. Goushi, J. Ribierre, T. Matsushima and C. Adachi, *Adv. Opt. Mater.*, 2016, **4**, 834–839.
103 Q. Liao, X. Jin, H. Zhang, Z. Xu, J. Yao and H. Fu, *Angew. Chem., Int. Ed.*, 2015, **54**, 7037–7041.
104 S. Varghese, S. K. Park, S. Casado, R. C. Fischer, R. Resel, B. Milián-Medina, R. Wannemacher, S. Y. Park and J. Gierschner, *J. Phys. Chem. Lett.*, 2013, **4**, 1597–1602.
105 M. Ichikawa, R. Hibino, M. Inoue, T. Haritani, S. Hotta, T. Koyama and Y. Taniguchi, *Adv. Mater.*, 2003, **15**, 213–217.
106 S. J. Yoon, J. W. Chung, J. Gierschner, K. S. Kim, M. G. Choi, D. Kim and S. Y. Park, *J. Am. Chem. Soc.*, 2010, **132**, 13675–13683.
107 D. Liu, J. Li, J. Liu, X. Lu, M. Hu, Y. Li, Z. Shu, Z. Ni, S. Ding, L. Jiang, Y. Zhen, X. Zhang, H. Dong and W. Hu, *J. Mater. Chem. C*, 2018, **6**, 3856–3860.
108 Q. Niu, Q. Zhang, W. Xu, Y. Jiang, R. Xia, D. D. C. Bradley, D. Li and X. Wen, *Org. Electron.*, 2015, **18**, 95–100.
109 S. Tavazzi, L. Silvestri, L. Miozzo, A. Papagni, P. Spearman, S. Ianelli, A. Girlando, A. Camposeo, M. Polo and D. Pisignano, *ChemPhysChem*, 2010, **11**, 429–434.
110 S. J. Yoon, S. Varghese, S. K. Park, R. Wannemacher, J. Gierschner and S. Y. Park, *Adv. Opt. Mater.*, 2013, **1**, 232–237.
111 S. K. Park, J. H. Kim, S. J. Yoon, O. K. Kwon, B. K. An and S. Y. Park, *Chem. Mater.*, 2012, **24**, 3263–3268.
112 J. Liu, H. Zhang, H. Dong, L. Meng, L. Jiang, L. Jiang, Y. Wang, J. Yu, Y. Sun, W. Hu and A. J. Heeger, *Nat. Commun.*, 2015, **6**, 10032.
113 Z. Wang, Q. Gao, Z. Zhang, J. Ren, J. De, X. Zhang, Z. Xu and H. Fu, *J. Mater. Chem. C*, 2018, **6**, 7994–8002.
114 M. Ichikawa, R. Hibino, M. Inoue, T. Haritani, S. Hotta, K. Araki, T. Koyama and Y. Taniguchi, *Adv. Mater.*, 2005, **17**, 2073–2077.
115 T. Nakagawa, S. Y. Ku, K. T. Wong and C. Adachi, *Chem. Commun.*, 2012, **48**, 9580–9582.
116 Z. Xu, Q. Liao, Q. Shi, H. Zhang, J. Yao and H. Fu, *Adv. Mater.*, 2012, **24**, OP216–OP220.
117 P. Morgante and R. Peverati, *Int. J. Quantum Chem.*, 2020, **120**, e26332.
118 A. J. Cohen, P. Mori-Sanchez and W. Yang, *Chem. Rev.*, 2012, **112**, 289–320.
119 J. M. Herbert, X. Zhang, A. F. Morrison and J. Liu, *Acc. Chem. Res.*, 2016, **49**, 931–941.
120 M. Lehnhardt, T. Riedl, T. Weimann and W. Kowalsky, *Phys. Rev. B: Condens. Matter Mater. Phys.*, 2010, **81**, 165206.
121 N. C. Giebink and S. R. Forrest, *Phys. Rev. B: Condens. Matter Mater. Phys.*, 2009, **79**, 073302.
122 A. V. Deshpande, A. Beidn, A. Penzkofer and G. Wagenblast, *J. Chem. Phys.*, 1990, **142**, 123–131.
123 R. C. Hilborn, *Am. J. Phys.*, 1982, **50**, 982–986.
124 Q. Zhang, W. Tao, J. Huang, R. Xia and J. Cabanillas-Gonzalez, *Adv. Photonics Res.*, 2021, **2**, 2000155.
125 S. Madayanad-Suresh, D. Hall, D. Beljonne, Y. Olivier and E. Zysman-Colman, *Adv. Funct. Mater.*, 2020, **30**, 1908677.
126 F. B. Dias, T. J. Penfold and A. P. Monkman, *Methods Appl. Fluoresc.*, 2017, **5**, 012001.
127 J. Lee, K. Shizu, H. Tanaka, H. Nakanotani, T. Yasuda, H. Kaji and C. Adachi, *J. Mater. Chem. C*, 2015, **3**, 2175–2181.
128 Z. Yang, Z. Mao, Z. Xie, Y. Zhang, S. Liu, J. Zhao, J. Xu, Z. Chi and M. P. Aldred, *Chem. Soc. Rev.*, 2017, **46**, 915.
129 S. G. Balasubramani, *et al.*, *J. Chem. Phys.*, 2020, **152**, 184107.
130 H. Nakanotani, T. Furukawa, T. Hosokai, T. Hatakeyama and C. Adachi, *Adv. Opt. Mater.*, 2017, **5**, 1700051.
131 H. Uoyama, K. Goushi, K. Shizu, H. Nomura and C. Adachi, *Nature*, 2012, **492**, 234–238.
132 R. Li and Z. Shuai, *Org. Electron.*, 2024, **132**, 107095.
133 J. Tao, J. P. Perdew, V. N. Staroverov and G. E. Scuseria, *Phys. Rev. Lett.*, 2003, **91**, 146401.
134 S. Grimme, J. Antony, S. Ehrlich and H. Krieg, *J. Chem. Phys.*, 2010, **132**, 154104.

135 C. A. Guido, E. Brémond, C. Adamo and P. Cortona, *J. Chem. Phys.*, 2013, **138**, 021104.
136 Y. Zhao and D. G. Truhlar, *J. Phys. Chem. A*, 2005, **109**, 5656–5667.
137 A. D. Boesea and J. M. L. Martin, *J. Chem. Phys.*, 2004, **121**, 3405–3416.
138 X. Chen, S. Deng, W. Zhang, P. Yin, W. Li and Z. Shuai, *J. Phys. Chem. A*, 2025, **129**, 2493–2509.
139 Z. Cheng, J. Liu, T. Jiang, M. Chen, F. Dai, Z. Gao, G. Ke, Z. Zhao and Q. Ou, *Adv. Opt. Mater.*, 2023, 2301093.
140 F. Weigend and R. Ahlrichs, *Phys. Chem. Chem. Phys.*, 2005, **7**, 3297–3305.
141 F. Weigend, *Phys. Chem. Chem. Phys.*, 2006, **8**, 1057–1065.
142 H. Y. S. Yu, X. He, S. H. L. Li and D. G. Truhlar, *Chem. Sci.*, 2016, **7**, 5032–5051.
143 A. D. Becke, *J. Chem. Phys.*, 1993, **98**, 1372–1377.
144 M. Reiher, O. Salomon and B. A. Hess, *Theor. Chem. Acc.*, 2001, **107**, 48–55.
145 J. P. Perdew, K. Burke and M. Ernzerhof, *Phys. Rev. Lett.*, 1996, **77**, 3865–3868.
146 J. Tao, J. P. Perdew, V. N. Staroverov and G. E. Scuseria, *Phys. Rev. Lett.*, 2003, **91**, 146401.
147 A. D. Becke, *Phys. Rev. A: At., Mol., Opt. Phys.*, 1988, **38**, 3098–3100.
148 J. P. Perdew, *Phys. Rev. B: Condens. Matter Mater. Phys.*, 1986, **33**, 8822–8824.
149 T. Fleetham, G. J. Li, L. L. Wen and J. Li, *Adv. Mater.*, 2014, **26**, 7116–7121.
150 J. Sun, H. Ahn, S. Kang, S. B. Ko, D. Song, H. A. Um, S. Kim, Y. Lee, P. Jeon, S. H. Hwang, C. Chu, S. Kim, D. Song and Y. You, *Nat. Photonics*, 2022, **16**, 212–218.
151 X. C. Hang, T. Fleetham, E. Turner, J. Brooks and J. Li, *Angew. Chem., Int. Ed.*, 2013, **52**, 6753–6756.
152 J. Li, F. Liang, Y. Zhao, X. Y. Liu, J. Fan and L. S. Liao, *J. Mater. Chem. C*, 2017, **5**, 6202–6209.
153 F. L. Yu, Y. J. Sheng, D. D. Wu, K. Qin, H. B. Li, G. H. Xie, Q. Xue, Z. Y. Sun, Z. Z. Lu, H. L. Ma and X. C. Hang, *Inorg. Chem.*, 2020, **59**, 14493–14500.
154 G. J. Li, L. Ameri, T. Fleetham, Z. Q. Zhu and J. Li, *Appl. Phys. Lett.*, 2020, **117**, 253301.
155 G. J. Li, S. Liu, Y. L. Sun, W. W. Lou, Y. F. Yang and Y. B. She, *J. Mater. Chem. C*, 2021, **10**, 210–218.
156 G. J. Li, K. Klimes, T. Fleetham, Z. Q. Zhu and J. Li, *Appl. Phys. Lett.*, 2017, **110**, 5.
157 G. J. Li, A. Wolfe, J. Brooks, Z. Q. Zhu and J. Li, *Inorg. Chem.*, 2017, **56**, 8244–8256.
158 L. Zhu, W. T. Xie, C. Y. Qian, W. Xie, K. Shen, A. Q. Lv, H. L. Ma, H. B. Li, X. C. Hang, W. Q. Li, S. J. Su and W. Huang, *Adv. Opt. Mater.*, 2020, **8**, 2000406.
159 H. J. Park, J. H. Jang, J. H. Lee and D. Hwang, *ACS Appl. Mater. Interfaces*, 2022, **14**, 34901–34908.
160 L. Zhu, C. W. Sha, A. Q. Lv, W. Xie, K. Shen, Y. M. Chen, G. H. Xie, H. L. Ma, H. B. Li and X. C. Hang, *Inorg. Chem.*, 2022, **61**, 10402–10409.
161 Y. M. Chen, C. Y. Qian, K. Qin, H. B. Li, X. B. Shi, Z. Z. Lu, H. L. Ma, T. S. Qin, X. C. Hang and W. Huang, *ACS Appl. Mater. Interfaces*, 2021, **13**, 52833–52839.
162 G. J. Li, X. D. Zhao, T. Fleetham, Q. D. Chen, F. Zhan, J. B. Zheng, Y. F. Yang, W. W. Lou, Y. N. Yang, K. Fang, Z. Shao, Q. Zhang and Y. She, *Chem. Mater.*, 2020, **32**, 537–548.
163 H. L. Ma, K. Shen, Y. P. Wu, F. Xia, F. L. Yu, Z. Y. Sun, C. Y. Qian, Q. M. Peng, H. H. Zhang, C. You, G. Xie, X. Hang and W. Huang, *Mater. Chem. Front.*, 2019, **3**, 2448–2454.
164 C. You, F. Xia, Y. Zhao, Y. Zhang, Y. J. Sheng, Y. P. Wu, X. C. Hang, F. Chen, H. L. Ma, K. Shen, Z. Sun, T. Ueba, S. Kera, C. Zhang, H. Zhang, Z. K. Chen and W. Huang, *J. Phys. Chem. Lett.*, 2018, **9**, 2285–2292.
165 T. Fleetham, L. Huang and J. Li, *Adv. Funct. Mater.*, 2014, **24**, 6066–6073.
166 G. J. Li, J. Ecton, B. Obrien and J. Li, *Org. Electron.*, 2014, **15**, 1862–1867.
167 R. Grotjahn and M. Kaupp, *J. Phys. Chem. A*, 2021, **125**, 7099–7110.
168 A. D. Becke, *J. Chem. Phys.*, 1993, **98**, 5648–5652.
169 A. V. Arbuznikov and M. Kaupp, *J. Chem. Phys.*, 2012, **136**, 014111.
170 T. Y. Li, J. Wu, Z. G. Wu, Y. X. Zheng, J. L. Zuo and Y. Pan, *Coord. Chem. Rev.*, 2018, **374**, 55.
171 L. Turcani, A. Tarzia, F. T. Szczypiński and K. E. Jelfs, *J. Chem. Phys.*, 2021, **154**, 214102.
172 C. Bannwarth, S. Ehlert and S. Grimme, *J. Chem. Theory Comput.*, 2019, **15**, 1652.
173 S. Grimme, *J. Comput. Chem.*, 2006, **27**, 1787–1799.
174 F. Weigend and R. Ahlrichxs, *Phys. Chem. Chem. Phys.*, 2005, **7**, 3297–3305.
175 E. Jansson, P. Norman, B. Minaev and H. Agren, *J. Chem. Phys.*, 2006, **124**, 114106.
176 K. Chao, K. Shao, T. Peng, D. Zhu, Y. Wang, Y. Liu, Z. Su and M. R. Bryce, *J. Mater. Chem. C*, 2013, **1**, 6800.
177 X. Li, J. Zhang, Z. Zhao, L. Wang, H. Yang, Q. Chang, N. Jiang, Z. Liu, Z. Bian, W. Liu, Z. Lu and C. Huang, *Adv. Mater.*, 2018, **30**, 1705005.
178 R. Wang, D. Liu, H. Ren, T. Zhang, X. Wang and J. Li, *J. Mater. Chem.*, 2011, **21**, 15494.
179 X. Ma, J. Liang, F. Bai, K. Ye, J. Xu, D. Zhu and M. R. Bryce, *Eur. J. Inorg. Chem.*, 2018, 4614.
180 J. Lee, H. Park, K. M. Park, J. Kim, J. Y. Lee and Y. Kang, *Dyes Pigm.*, 2015, **123**, 235.
181 J. Zhao, Y. Yu, X. Yang, X. Yan, H. Zhang, X. Xu, G. Zhou, Z. Wu, Y. Ren and W. Y. Wong, *ACS Appl. Mater. Interfaces*, 2015, **7**, 24703.
182 Y.-M. Jing and Y. Zheng, *New J. Chem.*, 2017, **41**, 3029.
183 J. H. Jou, *et al.*, *Adv. Funct. Mater.*, 2014, **24**, 555.
184 G. Tan, S. Chen, N. Sun, Y. Li, D. Fortin, W. Y. Wong, H. S. Kwok, D. Ma, H. Wu, L. Wang and P. D. Harvey, *J. Mater. Chem. C*, 2013, **1**, 808.
185 T. Y. Li, X. Liang, L. Zhou, C. Wu, S. Zhang, X. Liu, G. Z. Lu, L. S. Xue, Y. X. Zheng and J. L. Zuo, *Inorg. Chem.*, 2015, **54**, 161.
186 C. Adachi, R. C. Kwong, P. Djurovich, V. Adamovich, M. A. Baldo, M. E. Thompson and S. R. Forrest, *Appl. Phys. Lett.*, 2001, **79**, 2082.

